INDENTATION STUDIES ON A Zr-BASED BULK METALLIC GLASS

TANG CHUNGUANG
(*B. Eng., USTB*)

A THESIS SUBMITTED

FOR THE DEGREE OF MASTER OF SCIENCE

DEPARTMENT OF MATERIALS SCIENCE

NATIONAL UNIVERSITY OF SINGAPORE

2004

Acknowledgments

The author would like to express his sincere appreciation and gratitude to his thesis advisors, Dr. Zeng Kaiyang and A/P Li Yi, for their continuous guidance and understanding throughout this project. Their invaluable advice and support in the carrying out of the project enable the little pieces to fall into their rightful places.

Sincere appreciation is extended to all who helped in one way or another. A special word of thanks is to be given to Ms. Shen Lu and Ms. Tan Pei Ying (Joyce) for helping with all the project work, and to the students in Dr. Zeng's group who not only helped in the various areas of the project, but also opened the insight of the author by many helpful discussions. These helpful souls are Yang Shuang, Zhang Hongqing, Jiang Haiyan and many others. Sincere appreciation is also extended to members and students in Dr. Li's group who provided great help during the project. These helpful minds include Dr. Zhang Yong, Kong Huizi, Lee Mei Ling (Irene), Tan Hao, Wang Dong and many others.

The author would like to thank the Institute of Materials Research and Engineering and the National University of Singapore for providing scholarship to support the project.

Last but not least, a heartfelt appreciation to his wife for her support in every way, and all the friends who have prayed for the author and/or walked with him through the project.

Table of Contents

Summary

With advancements in bulk metallic glasses as promising structural materials, there has been an increasing interest in characterizing their mechanical properties. However, in traditional uniaxial tests such as tensile or compressive tests, metallic glasses generally fail catastrophically soon after their elastic limit. As an alternative way, indentation has been a widely used characterization method due to its ability to produce a stable stress field in bulk metallic glasses. Some interesting information has been obtained by using sharp indentations that produce some constant indentation strains in the specimens. However, spherical indentation, a technique able to produce various indentation strains and commonly applied to crystalline materials, has seldom been used to study bulk metallic glasses. Thus, it would be of interest to probe the mechanical properties of bulk metallic glasses with spherical indentation technique. In this project, the mechanical properties of bulk metallic glass $Zr_{52.5}Ti_5Cu_{17.9}Ni_{14.6}Al_{10}$ were studied using a spherical diamond indenter tip with radius of 200 μm and indentation load range of 10 to 240 N. The mean pressures of indentation were found to increase gradually to and saturate at 5.5 GPa as indentation loads increased. As the mean pressures reached the constant value, shear bands in spiral shape were found around the spherical indentation impressions on the free surface. These were discussed in the frame of contact mechanics on spherical indentation. Nanoindentations around the fully plastic spherical indentations were conducted to probe the influences of the residual spherical indentation impressions on the properties of specimens. Nanoindentation results revealed a reduction of apparent hardness around the residual spherical indentation. This might arise from the vanishment of pile-up around the nanoindentations nearby the spherical indentation, which was attributed to the interactions between the pre-introduced shear bands by the spherical indentation and

the new shear bands by nanoindentations. Such interactions were further investigated by using nanoindentations at low loading rates and were found to have influences on the serrated plastic flow behavior of bulk metallic glasses.

Keywords:

Bulk metallic glass, Mechanical properties, Hardness, Shear band, Spherical indentation, Nanoindentation.

List of Tables

List of Figures

Chapter 1 Introduction

1.1 Background

Metallic glasses, also known as amorphous alloys, glassy alloys or non-crystalline alloys, are alloys without any long-range atomic order. They are produced by rapid solidifications of the alloying constituents from liquid phases, so that the atomic configuration in their liquid phase is kept at lower temperatures.

Owing to their amorphous structures, metallic glasses possess unique behaviours. In general, metallic glasses exhibit higher tensile fracture strength (σ_f), higher Vickers hardness (H_V) and lower Young's modulus (E) than those of crystalline alloys. Some Fe-based metallic glasses have very good soft magnetic properties. Some metallic glasses are exceptionally corrosion resistant. For example, Mg-based metallic glasses show high resistance to hydrogen corrosion [1-2].

However, before the late 1980s, the dimensions of metallic glasses were limited to micrometer scale (usually less than 50 μm in thickness) due to the fact that high critical cooling rate (R_c) is required. After 1990, bulk metallic glasses (BMGs) with milimeter scale were found in multicomponent alloy systems with much lower critical cooling rates. In 1996, bulk $Pd_{40}Cu_{30}Ni_{10}P_{20}$ amorphous alloy was found with thickness as large as 72 mm [3].

The production of metallic glasses in bulk form has made them promising candidates for engineering materials, and stimulated extensive investigations on the mechanical properties of metallic glasses during the last decade. The mechanical properties of metallic glasses are highly dependent upon the stress status and

environmental temperature they encounter. At low stresses and high temperatures, the materials tend to deform homogeneously and show large plasticity, often accompanied by work softening. At high stresses and low temperatures, however, metallic glasses tend to deform inhomogeneously and exhibit little macroscopic plasticity under compressive and tensile tests.

Indentation technique is traditionally used to measure hardness. The indenter introduces a constrained, or stable stress field and thus can induce significant plastic deformation in the specimen. Due to this characteristic, indentation provides a method to investigate the plastic deformation behaviour of metallic glasses at room temperature. Research works have been done in this field using nanoindentation with sharp indenter tips [4-6]. In view of the fact that sharp indentation only introduces a constant strain in materials, in this work we will carry out blunt (spherical) indentations to investigate the mechanical properties of a Zr-based BMG under different indentation strains. On top of this, sharp nanoindentations will be conducted to probe the influences of blunt indentations on the materials.

1.2 Objectives

The main objective of the present study is to use spherical indentation technique to characterize the mechanical properties of a Zr-based BMG. The behaviours of the metallic glass under different indentation conditions will be investigated and the effect of the indentation on the surrounding material will be studied by using sharp nanoindentation.

1.3 Scopes and Organization of Thesis

Chapter 2 is the literature review on the history, processes and properties of metallic glasses. Previous work about indentations on metallic glasses will also be given in this chapter. It is then followed by an introduction to the indentation technique and its theory in Chapter 3. The introduction to the depth-sensing indentation systems, such as Ultra Micro Indentation System (UMIS, CSIRO, Australia) and Nano Indenter XP (MTS, USA), is also included in this chapter. The experimental procedures used in this project are described in Chapter 4, including basic material characterizations, conventional hardness measurement by spherical indentation, and nanoindentation characterization around the spherical indentation impressions. The part of results and discussion is included in Chapter 5. Finally, conclusions and recommendations for further work are given in Chapter 6.

References:

1. Inoue, A., *Materials Science and Engineering A*, **304-306**, 1 (2001).

2. Inoue, A., *Acta Materialia*, **48**, 279 (2000).

3. Inoue, A., in *Amorphous and Nanocrystalline Materials*, ed. by Inoue, A. and Hashimoto, K., Springer-Verlag New York, Inc., New York, 1 (2001).

4. Vaidyanathan, R., Dao, M., Ravichandran, G. and Suresh, S., *Acta Materialia*, **49**, 3781 (2001).

5. Kim, J. J., Choi, Y., Suresh, S. and Argon, A. S., *Science*, **295**, 654 (2002).

6. Schuh, C. A. and Nieh, T. G., *Acta Materialia*, **51**, 87 (2003).

Chapter 2 Literature Review

2.1 History of Metallic Glasses

Metallic glasses are alloys without long-range atomic order, i.e., without crystalline structure, and thus are also called amorphous alloys. In general, they are produced by rapid quenching of alloy melts.

The formation of metallic glasses by direct quenching from the melt was first reported in 1960 by Duwez and co-workers [1] in an Au-Si alloy. They adopted a "gun technique" to create a cooling rate up to 10^6 K/s and obtained an alloy with lack of Bragger's peak in its x-ray diffraction (XRD) pattern. Since then, a number of alloy systems have been used to form metallic glasses by quenching from melt; they were extensively reviewed by Davies [2]. There are several major groups of metallic glasses. The first group of metallic glass is the late transition metal-metalloid (TL-M) type; metalloids used include Group VIIB, Group VIII and Group IB noble metals. Examples of this group are Pd-$Si_{13\text{-}25}$, Fe-$B_{13\text{-}25}$, Ni-$B_{31\text{-}41}$ and Pt-$Sb_{34\text{-}36.5}$. The second major group is based on alloys of the type TE-TL, where TE is early transition metals (Ti, Zr, Nb, Hf, etc.) and TL is late transition metals (Fe, Co, Ni, Pd, etc.). Examples of this type are Cu-$Ti_{35\text{-}70}$, Cu-$Zr_{27.5\text{-}75}$ and Nb-$Ni_{40\text{-}66}$. Another major group includes binary and multicomponent alloys of Group IIA alkaline earth (AE) metals with certain B sub-group metals, with Group IV TE or with TL and Group IB noble metals. Examples are Ca-$Al_{12.5\text{-}47.5}$, Be-$Zr_{50\text{-}70}$ and Mg-$Zn_{25\text{-}32}$.

Except noble metal (such as Pd) based alloys, all the metallic glasses needed critical cooling rates above 10^4 K/s and this limited the dimensions of the materials to approximately 100 μm in thickness in earlier time. Though metallic glasses were

successfully used as soft magnetic materials and filler materials in brazing, the application of their high strength had been limited until the discovery of the BMGs in 1980s.

I. Nonferrous Metal Base	Year	Thickness $_{max}$ (mm)
Mg-Ln-M (Ln=lanthanide metal, M=Ni, Cu or Zn)	1988	10
Ln-Al-TM (TM=VI-VIII transition metal)	1989	10
Ln-Ga-TM	1989	10
Zr-Al-TM	1990	30
Ti-Zr-TM	1993	3
Zr-Ti-TM-Be	1993	25
Zr-Ti-Al-TM	1995	20
Pd-Cu-Ni-P	1996	72
Pd-Cu-B-Si	1997	10
II. Ferrous Group Metal Base	**Year**	**Thickness $_{max}$ (mm)**
Fe-(Al, Ga)-(P, C, B, Si, Ge)	1995	3
Fe-(Nb, Mo)-(Al, Ga)-(P, B, Si)	1995	3
Co-(Al, Ga)-(P, B, Si)	1996	1
Fe-(Zr, Hf, Nb)-B	1997	5
Co-(Zr, Hf, Nb)-B	1997	1
Ni-(Zr, Hf, Nb)-B	1997	1
Fe-(Co, Ni)-(Zr, Hf, Nb)-B	1997	6

Table 2-1 Alloy systems, years and maximum thicknesses of multicomponent alloys with high glass forming ability [3].

The size of 10 mm in thickness was obtained in a Pd-based metallic glass $Pd_{40}Ni_{40}P_{20}$ in 1984, but non-nobel metal-based BMGs were first reported in the late 1980s. In 1988 and 1989, BMGs with thickness of 10 mm were obtained in several multicomponent alloy systems, including Mg-Ln-TM, Ln-Al-TM and Ln-Ga-TM (TM=transition metal). Between 1990 and 1995, metallic glass systems Zr-AL-TM, Zr-Ti-TM-Be and Zr-Ti-Al-TM with thicknesses of 30, 25 and 20 mm were found. In 1996, large glass formation by water quenching was reported in Pd-Cu-Ni-P system

with diameter up to 72 mm, which is the largest size reported so far. The development history of BMGs was reviewed by Inoue [3] and summarized in Table 2-1.

2.2 Structure of Metallic Glasses

Before the discovery of metallic glasses, researchers had used X-ray, neutron and electron diffraction methods to characterize the structure of non-crystalline materials and proposed various structural models for non-crystalline materials. These models were used to describe the structures of metallic glasses and were reviewed by Chen [4]. Generally they may be classified into two types: discontinuous type and continuous random type.

The discontinuous type includes microcrystalline model and amorphous cluster model. The former interprets amorphous solids as inhomogeneous composites in which misoriented microcrystallites containing several hundred atoms are separated by less ordered non-crystalline atoms. The latter describes the material in a similar way but substitutes the microcrystallites in the former with non-crystallographic, highly ordered and low-energy atomic clusters that usually contain less than 50 atoms. The continuous random models describe the materials as homogeneous. Two typical models are the dense random packing of hard spheres (DRPHS) model and the continuous random network (CRN) model, in which tetrahedral units link together to form a continuous irregular three-dimensional network.

An important tool used in the diffraction methods to describe the structure of amorphous materials is the radial distribution function (RDF) $4\pi r^2\rho(r)$, where $\rho(r)$ is the average atomic density at the distance r from a reference atom. RDF indicates the number of atoms in a spherical shell of radius r having unit thickness and presents a statistical average projection of the structure onto one dimension. Another important

parameter is pair distribution function (PDF), $g(r)= \rho(r)/\rho_0$, where ρ_0 is the overall average density. For amorphous materials (liquid and glass), $g(r)$ has a peak value at a distance between 2 r_0 and 4 r_0, where r_0 is the radius of the reference atom, and reaches its asymptotic constant value (=1) at the correlation distance δ, beyond which the local correlation in the positions of nearby atoms is lost (Fig. 2-1).

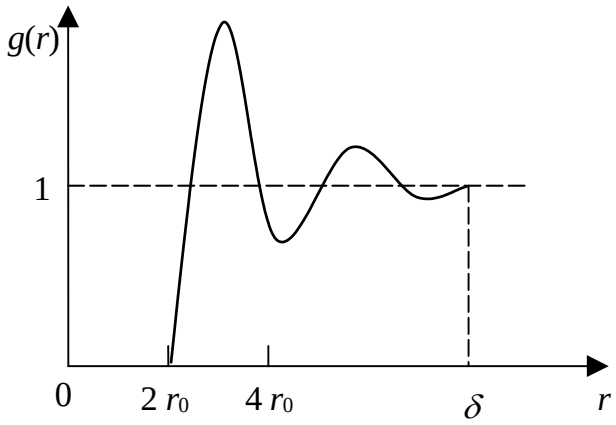

Fig. 2-1 Schematic PDF $g(r)$ for amorphous materials. $g(r)$ shows several peaks before it reaches the asymptotic constant 1.

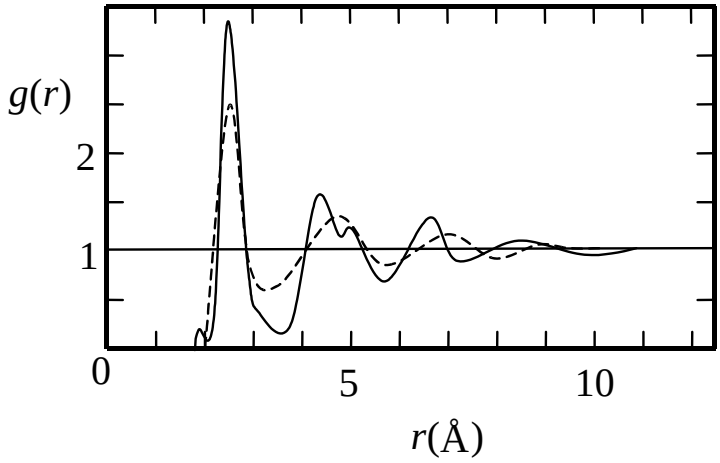

Fig. 2-2 The PDF $g(r)$ for amorphous Fe film (solid line) and liquid Fe (dashed line) [4].

Fig. 2-2 illustrates the PDF of amorphous Fe film, obtained by vacuum evaporation onto cooled substrates, and liquid Fe [4]. The oscillations in $g(r)$ for the amorphous Fe film have a larger amplitude and persist to a longer distance than those for the liquid Fe, indicating stronger short-range order in the amorphous Fe film. The PDF of the

amorphous Fe film is characterised by the splitting of the second peak into a main peak and a weak subpeak at larger *r*. The PDFs for amorphous Ni, Co, Mn and Au films are found to be very similar to that of amorphous Fe film. The phenomenon of splitting in the second PDF peak not only exists in amorphous pure metal films, but also exists in almost all of the metal-metalloid alloy glasses. The splitting phenomenon in metallic glasses is qualitatively in agreement with the DRPHS model, according to which the splitting of the second peaks in $g(r)$ with maxima at 1.73 and 2.0 sphere diameters is obtained [4].

Among metal-metal glasses, PDF data observed from rare earth-transition metals (RE-TMs) indicate that the nearest neighbour maxima are associated with well defined RE-RE, RE-TM and TM-TM nearest neighbour spacing. The PDFs obtained using x-ray anomalous scattering techniques for Zr-Cu glasses and $Zr_{70}(TM)_{30}$ (TM=Fe, Co, Ni and Pd) glasses exhibit following features [4]: (i) short interatomic distances of Zr-Zr and Zr-TM pairs result from a nearly empty *d* shell in Zr atoms through charge transfer, which obtains further evidence from the structural studies on Zr-Cu and Nb-Ni alloys where the interatomic distances of Zr-Zr and Nb-Nb pairs decrease with increasing Cu and Ni contents; (ii) the distribution functions of Zr-TM pairs have sharper first and second maxima than those of like-atom pairs, indicating preferred interactions of unlike-atom pairs; and (iii) minor constituent atoms (TM-TM) pairs show a hard contact, contrast to the metal-metalloid system where the minor constituent atoms (metalloids) are separated.

2.3 Glass Forming Ability (GFA)

Glass forming ability (GFA) indicates the ease for an alloy to form glass. BMGs found in multicomponent metal alloys with large differences in atomic sizes usually

have high GFA. In general, high GFA is obtained when the volume Gibbs free energy change ΔG is low during transformation from liquid to crystalline phase, which, according to

$$\Delta G = \Delta H - T \cdot \Delta S \qquad (2\text{-}1),$$

requires low ΔH and high ΔS. In Equation (2-1), ΔH is the enthalpy change and ΔS is the entropy change. The component multiplication causes high ΔS and low ΔH, which in turn reduce the homogeneous nucleation rate and crystalline growth rate. The differences in atomic sizes contribute to the high liquid/solid interfacial energy, which also in turn suppresses crystallization and leads to high GFA. Several parameters commonly used for indicating GFA are summarized below [5].

a) T_{rg} : The reduced glass temperature T_{rg} is defined as the ratio of the glass transition temperature T_g to melting temperature T_m. High GFA requires high viscosity at the supercooled liquid region, the temperature region between T_g and T_m, which in turn requires high T_{rg}.

b) ΔT_x: ΔT_x is the temperature interval between crystallization temperature (T_x) and T_g, indicating the resistence of metallic glasses to crystallization in the supercooled liquid region. In general, large ΔT_x is related to large GFA.

c) ΔT^*: ΔT^* is a parameter representing the fractional departure of the melting temperature, T_m, from the simple rule of mixture melting temperature T_m^{mix}. T_m^{mix} is defined as $\sum_i^n x_i T_m^i$, where x_i and $T_m{}^i$ are the mole fraction and melting point of the *i*th component of an *n*-component alloy. Many metallic glasses have values of ΔT^* >0.2.

d) K_{gl}: Defined as $(T_x - T_g)/(T_m - T_x)$, K_{gl} reprensents the thermal stability of a glass upon subsequent reheating, which is proportional to the ability of glass forming. In this approach, it is assumed that all glasses are in comparable states at T_g.

These parameters and some other criteria were reviewed by Li [5] and ΔT_x was pointed as a good indicator of GFA for easy glass forming alloys. Based on the observation of high GFA in multiple component alloys, Inoue [6] proposed three empirical rules for alloys with high GFA: (i) multicomponent systems consisting of more than three elements; (ii) significant difference in atomic size ratios above about 12% among the three main constituent elements; and (iii) negative heats of mixing among the three main constituent elements. Multicomponent alloys abiding by the three rules have higher degree of dense randomly packed atomic configurations, new local atomic configurations, which are different from those of the corresponding crystalline phases, and homogeneous atomic configuration of the multicomponents on a long-range scale. The difference in the densities between the as-cast amorphous and fully crystallized states of multicomponent alloys is only 0.30-0.54%, much smaller than that of about 2% for ordinary amorphous alloys [6]. Such small density differences indicate that the multicomponent amorphous alloys have higher dense randomly packed atomic configurations. X-ray scattering studies on the coordination numbers and atomic distances of each atomic pair of the multicomponent amorphous alloys reflect the existence of at least one atomic pair with significant difference in coordination numbers before and after crystallization, implying the necessity of long-range atomic rearrangements of atoms for the progress of crystallization as well as the difference in the local atomic configurations between the amorphous and crystalline phase. Contrary to ordinary amorphous alloys having the second peak splitting in

PDFs (refer to Fig. 2-2), multicomponent amorphous alloys, more like ordinary alloy liquids, show neither splitting of the second peak nor pre-peak at the first peak, indicating the homogeneous distribution of constituent elements on a long-range scale. All these produce high solid/liquid interfacial energy, which is favourable for the suppression of nucleation of a crystalline phase and for a higher GFA [6].

2.4 Preparing Methods

The formation of metallic glasses was first reported in $Au_{75}Si_{25}$ in 1960 by Duwez and co-workers [1] using so-called splat quenching or gun technique, which was able to produce a cooling rate of 10^6 K/s. In this process, a small liquid globule was propelled into small droplets by means of a shock tube and the droplets were sprayed into thin foil on a copper substrate. Samples so produced were irregular in shape with varying thicknesses from about 1 to 10 μm. Later, an improved piston and anvil technique could produce amorphous anvil foil with 15 to 25 mm in diameter and relatively uniform thickness of about 40 μm [4]. In early 1970s, continuous fabrication of metallic glasses in the form of ribbon was developed by using a technique of melt spinning, which involved the formation of a melt jet by the expulsion of molten alloy through an orifice and the impingement of this jet against a rapidly moving substrate surface, usually the outside surface of wheels [4, 7].

Since structural order in an atomically condensed film is determined largely by the surface mobility of the atoms, a highly disordered amorphous solid may be formed by sputtering and evaporation methods, where the atomic mobility is very low and the atoms condense at or near the point of impingement. A number of nominally pure amorphous metal films have been produced by evaporation and sputtering on to a substrate at very low temperatures. Both sputtering and evaporation methods are very

sensitive to deposition conditions, especially impurity contamination, which is believed to facilitate the formation of an amorphous atomic structure [4,7].

Metallic glasses may also be obtained by some other methods, such as chemical deposition, electro-deposition and ion implantation. Various transition metal-metalloid amorphous alloys have been produced by chemical deposition and electro-deposition. However, the deposition conditions and bath composition during the processes have strong influences on the precise composition of the product. The merit of ion implantation lies in the flexibility of introducing a broad variety of atomic species and obtaining impurity concentrations and distributions of particular interest [4,7].

Due to the relatively lower critical cooling rate required for multicomponent BMGs, now conventional casting methods are able to produce metallic glasses. The most frequently used techniques are described below [5].

a) Water quenching: During water quenching, a quartz tube containing the molten alloy is quenched directly into water. This method is convenient and is the most frequently used, but it is not proper for the alloy systems that can react with quartz tube, such as Mg-based alloys.

b) Chill casting: By chill casting, the molten alloys are directly cast into a copper mould with various dimensions and shapes, usually circular or rectangular. Sometimes, the copper mould is water-cooled. Chill casting is usually carried out in a closed chamber filled with argon as protective atmosphere.

c) High pressure die casting: Compared with conventional chill casting, high pressure die casting can provide higher cooling rate and thus produces larger size metallic glasses because it introduces good contact between molten alloy and the

mould. During casting, the molten alloy is injected into the copper mould by a plunger at high speed. Compared with conventional casting, this method can produce metallic glasses with less and smaller defects.

d) Suction casting: This method can achieve even higher cooling rate than pressure die casting does. In this procedure, the prealloyed ingot was remelted on a copper hearth in a protective atmosphere and then cast into the copper mould by withdrawing a piston at the center of the copper hearth at high speed.

e) Unidirectional solidification: This method can produce continuously long BMGs. In this method, zone melting is carried out in a protective atmosphere to continuously remelt the prealloyed ingot. An arc electrode serves as the heating source and the alloy is quenched by a copper hearth with water cooling.

2.5 Physical Properties

As quenched from the melt, metallic glasses have a large free volume in the materials and thus the density is lower than their crystalline counterparts. Traditional amorphous alloys with very high critical cooling rates generally possess about 2% lower density compared with their crystallized counterparts, while multicomponent BMGs have higher degree of dense randomly packed atomic configurations. Inoue [6] reported that the difference in the densities between the as-cast amorphous and fully crystallized states for Zr-based multicomponent BMGs lay in the range of 0.30-0.54%. Although the difference in densities between the amorphous and crystalline phases of multicomponent alloys was very small, studies on the densities of Zr- and Pd-based multicomponent BMGs revealed a systematic increase by structural relaxation, followed by a significant increase upon crystallization [3, 6].

Due to the lack of crystalline structure in metallic glasses, electrons are scattered more easily and thus the electrical resistivity of metallic glasses is relatively high. Inoue [3] indicated that, upon annealing, the electrical resistivity of Zr-based BMGs decreased with increasing temperatures before the glass transition, increased in the supercooled liquid region and dropped sharply upon crystallization. He also reported magnetic properties of Fe- and Co-based BMGs [8]. A ring-shaped bulk sample $Fe_{70}Al_5Ga_2P_{9.65}C_{5.75}B_{4.6}Si_3$ exhibited a high saturation magnetic flux density of 1.2 T, a low coercive force of 2.2 A/m and an extremely high initial permeability of 1.1×10^5 μ_e. The good soft magnetic properties were attributed to the unique magnetic domain structure, which was well arranged along the circumferential direction of the ring. Fe-Co-based multicomponent BMGs with high B concentration exhibited excellent high frequency permeability characteristics, with permeability 4 to 10 times higher than those for conventional Fe- and Co-based amorphous alloys at 1 MHz. The improved high frequency permeability characteristics were attributed to the high electrical resistivity caused by the high B concentration and the formation of a long-range homogeneous atomic configuration.

Metallic glasses have very low thermal expansion coefficient at the temperatures below T_g, but in the supercooled liquid region, the coefficient increases by several orders. Measurements for $Pd_{40}Cu_{30}Ni_{10}P_{20}$ amorphous alloy indicated that the thermal expansion coefficient increased from 8×10^{-6} K^{-1} in the range below 500 K to 2.6×10^{-2} K^{-1} between 602 and 613 K [3].

2.6 Mechanical Properties

The discovery of BMGs has made them promising structural materials and has stimulated investigations on their mechanical properties. Inoue [6] reviewed the

mechanical properties of La-, Mg-, Pd-, Zr-, Ti-, Fe-P- and Fe-B-based BMGs. Compared with crystalline alloys, BMGs possessed lower E, much higher σ_f and H_V. The ratio E/σ_f for crystalline alloys was about 130, while that for BMGs was only about 50. Three-point bending tests on Zr-Al-Ni-Cu and Zr-Ti-Al-Ni-Cu BMGs indicated that their flexural strengths were almost 2.0 to 2.5 times higher than those of crystalline Zr- and Ti-based alloys [6]. In addition to their high strengths, BMGs also show high fracture toughness. For example, fracture toughness of 55 MPa·mm$^{1/2}$ for amorphous alloy $Zr_{41.25}Ti_{13.75}Cu_{12.5}Ni_{10}Be_{22.5}$ was reported and this value compared well with that of high strength steel and Ti alloys [9].

Though metallic glasses have higher strength and elastic strain limits than crystalline metals, they generally show little elongation before fracture at room temperature [10]. During tensile and compression tests, they usually show large elastic strain, but after the elastic limit the plastic deformation is heavily localized in a single or a few shear bands which quickly propagate through the specimen, leading to a catastrophic failure. Such a plastic deformation through inhomogeneous shear bands is quite different from that of crystalline alloys and is a most interesting behaviour of metallic glasses. The studies on the plastic deformation of metallic glasses are briefly reviewed below.

2.6.1 Plastic Flow

Depending on the deforming conditions, the plastic deformation of metallic glasses can occur in two distinct regimes: homogeneous flow and inhomogeneous flow [11]. In the homogeneous flow, each volume element of the material contributes to the plastic strain and thus results in a uniform plastic deformation if the specimen is uniformly stressed. In the inhomogeneous flow, the plastic deformation is localized in

discrete, thin shear bands, leaving the material outside shear bands plastically undeformed. The strain inside the shear bands is very large and is accompanied by chemical disordering and dilation. The homogeneous flow occurs at low stress and high temperatures. The inhomogeneous flow usually occurs at high stress and low temperatures and may be observed in tensile tests, hardness tests and cold working processes. It is strain rate insensitive and is only dependent on temperature very weakly.

During the homogeneous flow, the plastic deformation of metallic glasses is strongly dependent on strain rate [12]. In the low strain rate region, accompanied by large plastic deformation, Newtonian flow behaviour occurs, i.e., m =1 in equation

$$\dot{\varepsilon} = \frac{1}{\mu}\sigma^m \qquad (2\text{-}2)$$

where $\dot{\varepsilon}$ is the strain rate, μ is the viscosity, σ is the shear stress and m is the strain rate sensitivity exponent. At high strain rates, the plastic deformation transits into non-Newtonian behaviour, i.e., the relationship between the strain rate and the shear stress becomes non-linear. The homogeneous plastic deformation in the supercooled liquid region is also dependent on the testing temperature. At low temperatures, a dramatic yield drop (or stress overshoot) phenomenon is often observed; it disappears at high temperatures with the flow stress decreased and the elongation increased.

Heilmaier [13] performed compressive tests on amorphous $Zr_{55}Cu_{30}Al_{10}Ni_5$ at both room temperature and elevated temperatures at constant strain rates between 3×10^{-3} and 1×10^{-5} s^{-1}. At room temperature, the metallic glass showed a high strength over 1.8 GPa and a plastic strain of up to 1% before catastrophic failure. At the elevated temperatures near T_g, the stress level for the amorphous alloy dropped to lower than 1

GPa, but the homogeneous flow resulted in extended plastic strain up to 30%. The deformation at elevated temperatures exhibited an obvious stress overshoot (stress peak), after which the stress declined to an almost constant level until failure. The peak stress decreased with decreasing strain rates, indicating that low strain rates led to the reduction of the overall flow stresses necessary for plastic deformation to occur. The phenomenon of stress overshoot was verified in creep tests under constant stresses, during which the creep rate decreased at low plastic strains and then gradually increased nearly to a constant. The minimum of creep rate was found to correspond to the stress peak during the tests at constant strain rates.

Kawamura et al [14] studied the deformation of BMG $Zr_{65}Al_{10}Ni_{10}Cu_{15}$ at high temperatures and found that, in the supercooled liquid region, the plastic deformation was strongly influenced by the strain rate. Newtonian behaviour, accompanied by high tensile elongations, only took place in low strain rate region; at high strain rates, the plastic flow became non-Newtonian. As the testing temperature decreased, the transition between Newtonian and non-Newtonian deformation took place at increasingly high strain rates. Nieh et al [12] studied the influences of testing temperature on tensile stress-strain behaviour of BMG $Zr_{52.5}Al_{10}Ti_5Cu_{17.9}Ni_{14.6}$ and found that the stress overshoot, which was readily observed around T_g (631 K), disappeared as the testing temperatures increased to higher than 683 K. They also studied stress-strain rate relationship for this alloy at 683 K and found that Newtonian behaviour took place in the low strain rate range ($<10^{-3}$ s^{-1}) and disappeared in the high strain rate range.

Chen et al [15] proposed that the stress overshoot was a result of rapid increase in the free volume during high strain rate deformation. Upon yielding, the excessive free volume redistributed quickly through local atomic rearrangement and resulted in the

observed yield drop or stress overshoot. Since the creation of excessive free volume and the subsequent annihilation were kinetic processes, the stress overshoot was both temperature and strain rate dependent. Later, Nieh et al [12] attributed the observed non-Newtonian behaviour in $Zr_{52.5}Al_{10}Ti_5Cu_{17.9}Ni_{14.6}$ at high strain rates to concurrent nanocrystallization during deformation. They argued that both nanocrystallization and free volume creation, both temperature and strain rate, affected the plastic flows in metallic glasses, and that a high strain rate and low temperature (near T_g) condition contributed to non-Newtonian flow.

Based on the macroscopic similarity of the sharp surface offsets produced by the shear bands to the slip lines observed after plastic deformation of single crystals, some researchers proposed dislocation motion to explain the phenomenon of inhomogeneous flow in metallic glasses [16-17]. The main problem about these dislocation models is whether these dislocation stress fields actually govern inhomogeneous flow. Computer and bubble raft modelling indicated that the plastic flow in deformation at high stresses was indeed controlled by various localized shear rearrangements, but these were different from extended line defects, such as dislocations [18-19]. On the macroscopic level, the dislocation models could not explain why the flow localized into a few shear bands and then resulted in fracture with characteristic vein-like morphology along the shear bands [11].

The localization of shear bands may be accounted for by any model that leads to a strong softening or reduction of the viscosity in the shear bands. Such a viscosity reduction localizes the plastic deformation in the shear bands and weakens the bands against fracture. The lowered viscosity also gives rise to the decrease in chemical order and density.

Two hypotheses were developed to explain the viscosity reduction for metallic glasses [20]. The first one was the free volume model, which suggested that the formation of free volume during deformation decreased the viscosity within the shear bands and the density of metallic glasses. Spaepen and Turnbull [21] pointed out that a stress concentrator, such as a micro crack, could produce enough extra free volume and cause a large viscosity drop. Later, Spaepen [22] studied the steady-state inhomogeneous flow in metallic glasses and proposed that, after the shear band was initiated at the stress concentrator, the softening in the shear band could be sustained by a balance process based on the competition between stress-driven creation and diffusional annihilation of free volume. Subsequently, Steif et al [23] extended Spaepen's work by analysing the establishment of inhomogeneous flow as a transient (or time-dependent) problem, together with the requirements for localization of the plastic strain. They derived an expression for the stress at which catastrophic softening due to free volume creation occurred during uniform shearing a homogeneous body at constant applied strain rates. It also became apparent that the shear bands formed so quickly that the steady state was probably never established.

The second hypothesis to explain the reduction of viscosity in shear bands was the adiabatic heating model, which contended that local adiabatic heating in the shear bands increased the temperature beyond the glass transition temperature, or even up to the melting temperature, and decreased the viscosity sharply. This idea was proposed in 1972 by Leamy et al [24], who attributed the vein pattern morphology of fracture surfaces to adiabatic heating in the deformed region. Later, Liu et al [25] observed sparking from Zr-based BMGs during the moment of fracture in tensile tests and found liquid droplets on the fracture surfaces. Assuming that all of the elastic strain energy stored in the sample was released as heat on the fracture plane, they estimated a

temperature increase of up to 900 K. This hypothesis gained support from the results of dynamic compression tests on a Zr-based metallic glass by Bruck et al [26], who found that the temperature near the melting point might be reached upon the failure of the metallic glass. Recent work of Flores and Dauskardt [27] showed that the local heating associated with crack tip plasticity in $Zr_{41.25}Ti_{13.75}Ni_{10}Cu_{12.5}Be_{22.5}$ metallic glass was well below the critical value for local melting. The maximum increase in temperature they measured was 54 K, however, they suggested that this low temperature increase could lead to sufficient viscosity reduction and the characteristic vein-like fracture surface morphologies. Wright et al [20] made quantitative measurements of the serrated plastic flow during uniaxial compression on $Zr_{40}Ti_{14}Ni_{10}Cu_{12}Be_{24}$ and predicted the temperature increase due to local adiabatic heating in a single shear band. Their results showed that the temperature increases were insufficient to reach the glass transition temperature and suggested that it was unlikely for localized heating to be the primary cause of flow localization. They argued that the localization of shear bands was more likely to be caused by the changes in viscosity associated with the increased free volume in the shear bands.

2.6.2 Shear Bands

Highly localised shear bands are the form of inhomogeneous deformation of the metallic glasses, which is quite unique compared with the deformation of crystalline metals and alloys. For polycrystalline metals and alloys, the plastic deformation is mainly influenced by shear stresses and characterized by Von Mises model, i.e., the deformation is not affected by the hydrostatic stresses. For the plastic deformation of metallic glasses, however, the hydrostatic stress-dependent Mohr-Coulomb model applies [28]. During tensile and compressive tests, the fracture plane is dominated by a major shear band that deviates from the maximum shear stress plane slightly [20, 29].

The load status also influences the behaviour of shear bands. During tensile tests, usually a few shear bands form and result in failure shortly after the onset of yielding, while during uniaxial compression or bending, multiple shear bands may form.

Spaepen and Turnbull [21] pointed out that the dilatation by stress concentrators, such as micro cracks and notches, could cause a large viscosity drop and initiate a shear band. Experimentally, shear bands were found to initiate from the tip of the micro cracks in metallic glasses. Pekarskaya et al [30] studied the propagation of shear bands in metallic glass based composite $Zr_{56.3}Ti_{13.8}Cu_{6.9}Ni_{5.6}Nb_5Be_{12.5}$ using in-situ straining transmission electron microscopy (TEM). In the glass phase, they observed sheared regions at the tips of cracks and crack branches, as well as in the narrow region around the cracks.

Li et al [31] compared the structure of shear bands with that of underformed regions in BMG $Zr_{57}Ti_5Cu_{20}Ni_8Al_{10}$ using quantitative high resolution TEM and observed void-like defects, approximately 1 nm in diameter and at a concentration of one in 100 nm^3, in the shear bands after plastic deformation. They proposed that these defects arose from the coalescence of excess free volume upon the cessation of flow and indicated that the free volume coalescence was thermodynamically possible. Wright et al [32] investigated the possibility of void nucleation from the coalescence of excess free volume in shear bands of metallic glass $Zr_{41.2}Ti_{13.8}Cu_{12.5}Ni_{10}Be_{22.5}$. By modelling the structure of the shear band as hypothetical glass solidified at some temperature above the glass transition temperature, they calculated the excess free energy of the shear band as a function of excess free volume. The results of their modelling indicated that any free volume generated in a shear band during deformation was highly unstable and spontaneously formed nanometer-scale voids.

In the shear bands, there are large strains, accompanied by chemical disordering and dilatation. Such flow-induced dilatation may increase the atomic diffusion mobility dramatically and may even cause the formation of nanocrystalline in the shear bands [33]. Chen et al [34] showed that severe bending of thin ribbons of an Al-based metallic glass led to nucleation of nanocrystallites in the induced shear bands. He et al [35] found that high-energy ball milling of thin ribbons of Al-based metallic glasses could induce nanocrystallites. As pointed out by Kim et al [33], ball milling produced highly complex and uncontrolled stress states, and possibly produced substantial local heating, which could thermally anneal the metallic glass. To investigate the effect of quasi-static deformation on nanocrystallization behaviour in the shear bands, they conducted nanoindentation experiments on metallic glass $Zr_{52.5}Cu_{17.9}Ni_{14.6}Al_{10}Ti_5$ and detected Zr_2Ni nanocrystallites with diameters ranging from 10 to 40 nm both along the faces of the indenter and in the region beneath the indenter tip, where the most severe deformation occurred. They believed that these nanocrystallites resulted from the flow dilatation inside the shear bands and the attendant, radically enhanced, atomic diffusional mobility inside the actively deforming shear bands.

Hufnagel et al [36] investigated the behaviour of shear bands in the composite $(Zr_{70}Cu_{20}Ni_{10})_{82}Ta_8Al_{10}$ with amorphous matrix and Ta-rich particles of around 10 μm in diameter [29]. When the specimens began to yield during compression tests, small shear bands initiated near the crystalline particles, which likely produced stress concentrations due to the large difference in the elastic modulus between the particles and the amorphous matrix. On the other hand, at large strains, the particles were found to inhibit shear band propagation by defecting the shear bands. Due to the interaction between the shear bands and the particles, the composite showed substantially larger plastic strain than metallic glasses did.

Xing et al [37] studied the branching behaviour of shear bands in BMGs. They compared the results of compression tests on metallic glasses $Zr_{59}Ta_5Cu_{18}Ni_8Al_{10}$ and $Zr_{57}Ti_5Cu_{20}Ni_8Al_{10}$ and found that the Ta-containing metallic glass showed much larger plastic strain, up to 6.4%. Such a large increase in the plastic strain was attributed to shear band branching, which made it more difficult for a propagating shear band to result in a crack and failure because the strain in any one branch was much smaller than that in a single, unbranched shear band. Their further investigation of the structures of these alloys showed that the presence of Ta enhanced the short- and medium-range order in the amorphous alloys [36]. They believed that such an enhanced order might interact with a propagating shear band and defect or bifurcate the latter.

2.6.3 Indentation Investigation on Metallic Glasses

Indentation may introduce a constrained or stable stress field and thus provides a way to characterize multiaxial plastic deformation of BMGs at room temperature. Some work has been done to investigate the mechanical behavior of BMGs through sharp indentation.

Vaidyanathan et al [28] conducted Berkovich nanoindentations and finite element simulations on $Zr_{41.25}Ti_{13.75}Cu_{12.5}Ni_{10}Be_{22.5}$ and proposed the yield criterion in the metallic glass. In materials, generally two yield criteria apply to predict the beginning of plastic deformation. One is hydrostatic-component-independent Von Mises yield criterion, which is stated as follows:

$$(\sigma_1 - \sigma_2)^2 + (\sigma_2 - \sigma_3)^2 + (\sigma_3 - \sigma_1)^2 = 2Y^2 \qquad (2\text{-}3)$$

where σ_1, σ_2 and σ_3 are the principal stresses and Y is the yield strength measured in a uniaxial tension test. Alternatively, Mohr-Coulomb criterion assumes that the plastic flow is influenced by the local normal stress and is generally written as follows:

$$\tau_c = \kappa_0 - \alpha\sigma_n \qquad (2\text{-}4)$$

where τ_c is the shear stress on the slip plane at yielding, κ_0 and α are constants and σ_n is the stress component normal to the slip plane. Upon comparing the indentation load-depth (*P-h*) relationship with finite element simulation results, they found that Mohr-Coulomb yield criterion applied in metallic glasses.

Kim et al [33] conducted quasi-static nanoindentations on $Zr_{52.5}Cu_{17.9}Ni_{14.6}Al_{10}Ti_5$ at room temperature and explored the shear bands by use of TEM. They found that nanocrystallites, same as those formed during annealing without deformation, nucleated in and around the shear bands and attributed the nanocrystallization to the high atomic mobility caused by flow dilatation in the shear bands.

Schuh and Nieh [38] conducted nanoindentations on Pd- and Zr-based BMGs at loading rates from 0.02 to 300 mN/s. They found that stepped *P-h* curves, corresponding to the serrated flow during nanoindentations, occurred at very low loading rates but were completely suppressed at high strain rates. These results were attributed to the kinetic limitation for shear bands. When the applied loading rate was low, a single shear band could rapidly accommodate the deformation and thus serrated flow occurred. In contrast, when the loading rate exceeded the rate of relaxation by a single shear band, multiple shear bands had to operate simultaneously and led to smooth *P-h* curves.

2.7 Summary

The researches on the mechanical behaviours of metallic glasses had been limited due to the small sample size of conventional metallic glasses. The development of BMGs in the late 1980s has enabled promising applications of metallic glasses as structural materials and has triggered a wide range of researches on their mechanical properties. BMGs have extremely high strength and very good elasticity, however, they generally fail catastrophically after their yield points during uniaxial deformations. To explore the plastic deformation behaviours of BMGs, researchers have employed the technique of indentation to produce a stable severe stress field in the materials and have obtained much useful information. In this project, the technique of indentation will be employed to study the mechanical behaviours of a Zr-based BMG. We will conduct indentation experiments on the metallic glass with a spherical indenter tip, which is able to produce a gradually growing stress field in the metallic glass. We will also use sharp indenter tips, which produce a constant strain in the material, to investigate the influences of the spherical indentation on the mechanical properties of BMGs.

Reference:

1. Jun, W. K., Willens, R. H. and Duwez, P., *Nature*, **187**, 869 (1960).

2. Davies, H. A., in *Amorphous Metallic Alloys*, ed. by Luborsky, F. E., Butterworth, London, 8 (1983).

3. Inoue, A., in *Amorphous and Nanocrystalline Materials*, ed. by Inoue, A. and Hashimoto, K., Springer-Verlag New York, Inc., New York, 1 (2001).

4. Chen, H. S., *Reports on Progress of Physics*, **43**, 353 (1980).

5. Li, Y., *Journal of Materials Science and Technology*, **15**, 97 (1999).

6. Inoue, A., *Acta Materialia*, **48**, 279 (2000).

7. Liebermann, H. H., in *Amorphous Metallic Alloys*, ed. by Luborsky, F. E., Butterworth, London, 26 (1983).

8. Inoue, A., *Materials Science and Engineering A*, **304-306**, 1 (2001).

9. Hertzberg, R. W., *Deformation and Fracture Mechanics of Engineering Materials*, John Wiley and Sons, New York (1989).

10. Kimura, H. and Masumoto, T., in *Amorphous Metallic Alloys*, ed. by Luborsky, F. E., Butterworth, London, 187 (1983).

11. Spaepen, F. and Taub, A. I., in *Amorphous Metallic Alloys*, ed. by Luborsky, F. E., Butterworth, London, 231 (1983).

12. Nieh, T. G., Wadsworth, J., Liu, C. T., Ohkubo, T. and Hirotsu, Y., *Acta Materialia*, **49**, 2887 (2001).

13. Heilmaier, M., *Journal of Materials Processing Technology*, **117**, 374 (2001).

14. Kawamura, Y., Nakamura, T. and Inoue, A., *Scripta Materialia*, **39**, 301 (1998).

15. Chen, H. S., Kato, H. and Inoue, A., *Materials Transactions*, **42**, 597 (2001).

16. Gilman, J. J., *Journal of Applied Physics*, **44**, 675 (1973).

17. Li, J. C. M., in *Metallic glasses*, ed. by Gilman, J. J. and Leamy, H. J., American Society of Metals, Cleveland, Ohio, 224 (1976).

18. Kobayashi, S., Maeda, K. and Takeuchi, S., *Acta Metallurgica*, **28**, 1641 (1980).

19. Argon, A. S. and Kuo, H. Y., *Materials Science and Engineering*, **39**, 101 (1979).

20. Wright, W. J., Saha, R. and Nix, W. D., *Materials Transactions*, **42**, 642 (2001).

21. Spaepen, F. and Turnbull, D., *Scripta Metallurgica*, **8**, 563 (1974).

22. Spaepen, F., *Acta Metallurgica*, **25**, 407 (1977).

23. Steif, P. S., Spaepen, F. and Hutchinson, J. W., *Acta Metallurgica*, **30**, 447 (1982).

24. Leamy, H. J., Chen, H. S. and Wang, T. T., *Metallurgical Transactions*, **3**, 699 (1972).

25. Liu, C. T., Heatherly, L., Easton, D. S., Carmichael, C. A., Schneibel, J. H., Chen, C. H., Wright, J. L., Yoo, M. H., Horton, J. A. and Inoue, A., *Metallurgical and Materials Transactions A*, **29A**, 1811 (1998).

26. Bruck, H. A., Rosakis, A. J. and Johnson, W. L., *Journal of Materials Research*, **11**, 503 (1996).

27. Flores, K. M. and Dauskardt, R. H., *Journal of Materials Research*, **14**, 638 (1999).

28. Vaidyanathan, R., Dao, M., Ravichandran, G. and Suresh, S., *Acta Materialia*, **49**, 3781 (2001).

29. Mukai, T., Nieh, T. G., Kawamura, Y., Inoue, A. and Higashi, K., *Intermetallics*, **10**, 1071 (2002).

30. Pekarskaya, E., Kim, C. P. and Johnson, W. L., *Journal of Materials Research*, **16**, 2513 (2001).

31. Li, J., Spaepen, F. and Hufnagel, T. C., *Philosophical Magazine A*, **82**, 2623 (2002).

32. Wright, W. J., Hufnagel, T. C. and Nix, W. D., *Journal of Applied Physics*, **93**, 1432 (2003).

33. Kim, J. J., Choi, Y., Suresh, S. and Argon, A. S., *Science*, **295**, 654 (2002).

34. Chen, H., He, Y., Shiflet, G. J. and Poon, S. J., *Nature*, **367**, 541 (1994).

35. He, Y., Shiflet, G. J. and Poon, S. J., *Acta Metallurgica et Materialia*, **43**, 83 (1995).

36. Hufnagel, T. C., Fan, C., Ott, R. T., Li, J. and Brennan, S., *Intermetallics*, **10**, 1163 (2002).

37. Xing, L. Q., Li, Y., Ramesh, K. T., Li, J. and Hufnagel, T. C., *Physical Review B*, **64**, 180201 (2001).

38. Schuh, C. A. and Nieh, T. G., *Acta Materialia*, **51**, 87 (2003).

Chapter 3 Indentation

3.1 Concept of Hardness

The concept of hardness has been a very old subject of consideration by scientists and engineers. However, as O"Neill [1] said, the hardness "like the storminess of seas, is easily appreciated but not readily measured for one would hope to express it in terms of fundamental units". Various definitions of hardness were proposed, such as that hardness implied the ability to unyield to the touch, and that it indicated the resistance to penetration or permanent deformation. Historically, hardness measurements fell into three main categories: scratch hardness, indentation hardness, and rebound or dynamic hardness [1]. Scratch hardness is the oldest form of hardness measurement and has been widely used by mineralogists. It depends on the ability of one solid to scratch another or to be scratched by another solid. This method involves a complicated function of the elastic, plastic, and frictional properties of the surfaces and is not suitable for a theoretical analysis. In static indentation, the hardness is determined by the load and the size of the permanent indentation impression formed in the surface of the materials to be examined. The indentation hardness may in general be expressed in terms of the plastic and, to a less extent, the elastic properties of the examined materials. Dynamic measurements involve an indenter dropped on to the surface of the materials concerned and the hardness is expressed in terms of the height of rebound of the indenter, or in terms of the energy of impact and the size of the remaining indentation. Compared with dynamic measurements, static hardness measurements reduce the number of test variables to a manageable level.

Based on the results of static and dynamic experiments, Hertz [2], in 1881, postulated that an absolute value for hardness was the least value of pressure beneath a

spherical indenter necessary to produce a permanent set at the centre of the area of contact. Subsequently, various hardness testing methods based on this proposal with the removing of some practical difficulties evolved [1, 3]. One of them is Brinell hardness test using a spherical indenter where Brinell hardness number (B. H. N.) is expressed as the ratio of the load to the curved contact area of indentation. The B. H. N. is not a good physical concept for it does not represent the mean pressure over the contact surface of the indentation. Another is Meyer hardness, which is similar to Brinell hardness except that the projected contact area rather than the actual curved surface area is used to determine the hardness. Meyer hardness is equal to the mean pressure and is applicable for conical and pyramidal indenters. Now the generally accepted concept of hardness results from Meyer's method and is expressed as

$$H = \frac{P_{\max}}{A} \qquad (3\text{-}1),$$

where H is the hardness, P_{max} is the maximum load applied and A is the projected contact area at P_{max}. After the load and indenter are removed, the material will recover elastically in the vertical direction, which is referred to as "shallowing" in the hardness literature [3]. For spherical indentation, this causes a larger curvature radius of the residual impression than that of the indenting sphere. The diminution in the chordal diameter of the indentation is small after the load is removed, usually less than a few percent. In conventional hardness tests, A is usually substituted by the projected contact area after the load is removed.

3.2 Indenter Geometries and Geometrical Similarity

Indenters can generally be divided into two types: sharp indenters and blunt indenters. The sharp indenters include conical indenters and pyramidal indenters

(Vickers, Berkovich and Knoop). The blunt indenters generally refer to spherical indenters and flat-ended punches.

For a pyramidal or conical indenter, the ratio of the contact diagonal length or contact circle diameter to the contact depth, d/h_c, remains constant for increasing indentation load or depth, as shown in Fig. 3-1 (a). This property is called geometrical similarity [4]. In the figure, the apex angle of the conical indenter is α and the angle of indentation is 180°-α. For a geometrically similar indentation, the indentation angle is a constant and the specimen is stressed or strained to the same degree, independent of the applied load. This means that the hardness obtained by sharp indentation is generally independent of the indentation depth and load.

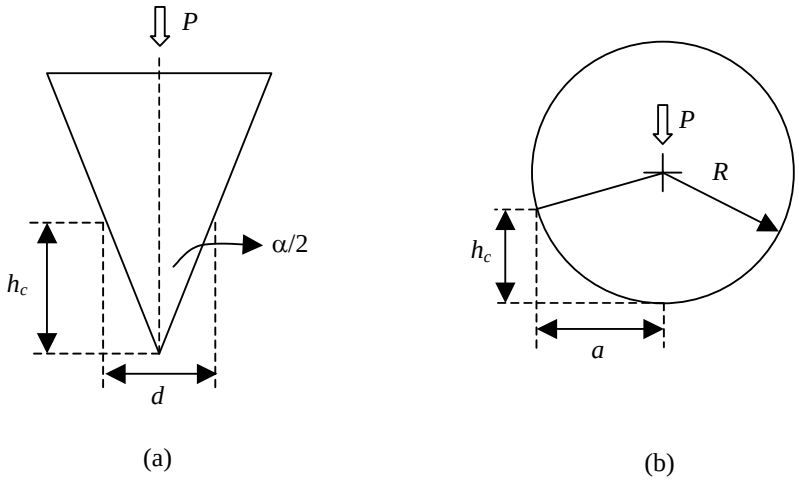

Fig. 3-1 (a) geometrical similarity of a conical indenter; (b) dissimilarity of a spherical indenter. *P* is the applied load.

A spherical indenter, however, does not possess such a property. The ratio of the contact circle radius to the contact depth, a/h_c, decreases with the applied load increased, as shown in Fig. 3-1 (b). Increasing the load on the spherical indenter is equivalent to decreasing the apex angle of the conical indenter, i.e., increasing the indentation angle. The strain in spherical indentation is defined as a/R, where R is

the indenter radius. The indentation strain increases with the applied load in spherical indentations. However, geometrical similarity can occur in spherical indentations with indenters of different radii as long as a/R remains constant [4].

Nowadays the frequently used sharp indenters are Berkovich and Vickers indenters partially because it is easier to make a pyramidal indenter with a sharp tip than a conical one. In this case, the triangle-base pyramidal Berkovich indenter can more easily achieve a sharp tip than the square-base pyramidal Vickers indenter does. This is simply because the edges of three-sided pyramid meet at a point rather than a line that occurs in the case of four-sided pyramid. The geometric parameters of Berkovich and Vickers indenters are shown in Fig. 3-2 and Fig. 3-3. Berkovich indenter is a three-sided pyramid with a semi apex angle of 65.3°. Vickers indenter is a square-based pyramid with an angle of 136° between faces.

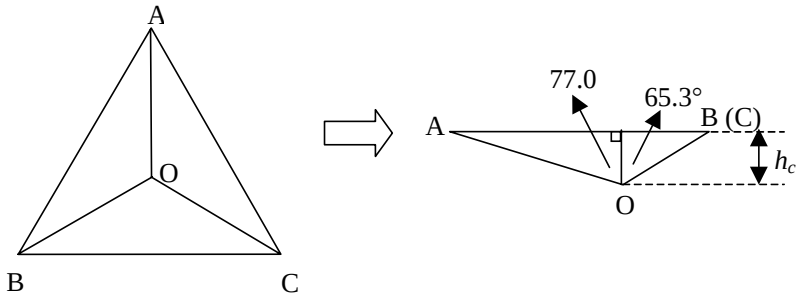

Fig. 3-2 Berkovich indenter tip geometric parameters. (a) top view; (b) side view. In the figure, AB=BC=CA and AO=BO=CO. Projected contact area=24.5 $h_c^{\ 2}$.

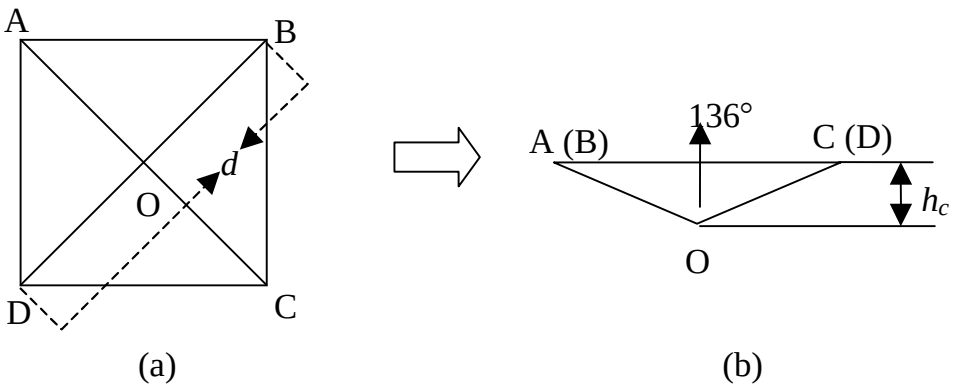

Fig. 3-3 Vickers indenter tip geometric parameters. (a) top view; (b) side view. In the figure, AB=BC=CD=DA and AO=BO=CO=DO. Projected contact area=24.5 $h_c^{\ 2}$.

3.3 Depth Sensing Indentation

In conventional hardness tests, the load ranges from ten to several hundred Newton. Then, the need to probe smaller volume materials leads to the development of micro hardness testing with loads that do not exceed 10 N. Typically, micro hardness tests are made with loads from 1 to 5 N. In the early 1980s, the measurement of mechanical properties of thin films and surface layers using sub-micro hardness testing gained increasing interests. Such tests, usually called nanoindentations, possess a typical load range below 0.5 N.

In conventional indentations, the contact area is determined using optical microscope after the load is removed. However, this practice can result in pronounced inaccuracy in micro indentation and nanoindentation since the contact areas in such cases are very small. During tests at this stage, depth sensing indentation technique is employed. With this technique, the data of load and penetration depth are collected throughout the loading and unloading processes. In addition to giving more accurate contact areas, this technique provides information about the elastic properties and time-dependent plastic properties of the materials.

3.3.1 Load-Displacement Curve Interpretation

An indentation test involves a complete cycle of loading and unloading, as shown in Fig. 3-4. The depth represents the total displacement of the indenter into the specimen relative to the original specimen surface. For most materials the loading process consists of both elastic and plastic deformation, but the unloading is only a recovery process of the elastic displacements. Thus, the unloading process can be analysed by modeling it to an elastic contact problem that an elastic half space is indented by a rigid punch relating the projected contact area at the peak load to the elastic modulus. The problem of elastic contact was originally considered by Boussinesq [5] and Hertz [2] in the late 19th century. They were concerned with the stresses and displacements between two elastic solids in contact and their solutions formed the basis of many of the experimental work and theoretical work in the indentation of materials with rigid and non-rigid indenters of various shapes. Hertz gave an equation relating the force (*P*) to the depth (*h*) of an indentation on a semi-infinite elastic half space by a rigid sphere:

$$P = \frac{8\sqrt{R}}{3}\frac{E}{1-\upsilon^2}h^{3/2} \qquad (3\text{-}2),$$

where *R* was the sphere radius, *E* and υ were the Young's modulus and Poisson's ratio of the material, respectively. Hertz's work in the elastic contact between two spherical surfaces with different radii provided a framework in the indentation with non-rigid indenters.

In 1939, Love [6] obtained the relationship between the force and depth of a rigid cone indenting an elastic half-space using Boussinesq's potential function method:

$$P = \frac{2E\tan\theta}{\pi(1-\upsilon^2)}h^2 \qquad (3\text{-}3),$$

where θ was the semi-included angle of the rigid cone. Later Sneddon [7-9] derived general relationships among the load, displacement and contact area for any indenter that could be described as a solid of revolution of a smooth function. For many simple indenter geometries, the load displacement relationships could be conveniently written as

$$P = \alpha h^m \qquad (3\text{-}4),$$

where P was the applied load, h was the elastic displacement of the indenter and α and m were constants. α contained geometric constants, elastic modulus and Poisson's ratio of both the sample and the indenter. The exponent, m, was related to the indenter geometry and values for some common indenter geometries were m=1 for flat cylinders, m=2 for cones, m=1.5 for balls in the limit of small displacements, and m=1.5 for paraboloids of revolution.

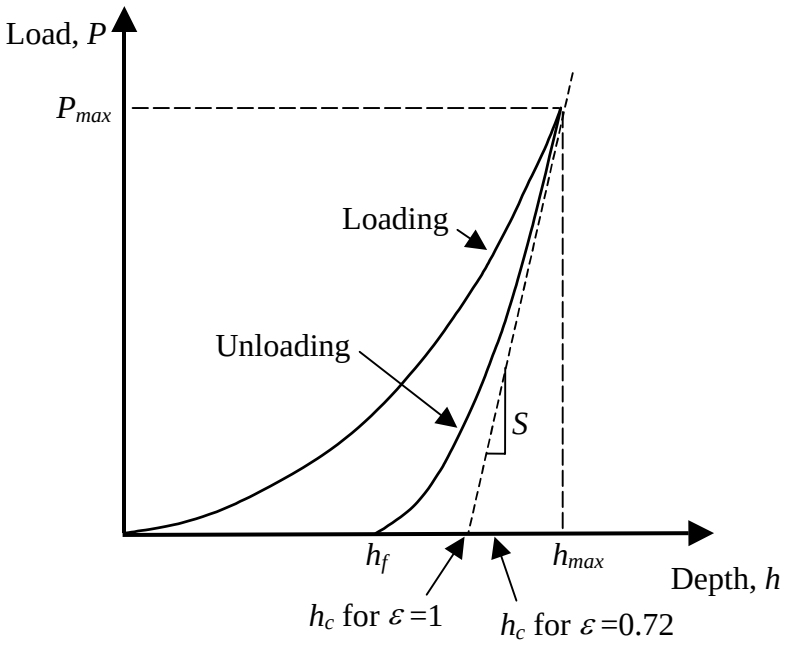

Fig. 3-4 Schematic representation of load versus indenter displacement. P_{max}: the peak load; h_{max}: the indenter displacement at the peak load; h_c: the depth intercept of the unloading curve tangent at P_{max}; h_f: the final depth of the contact impression after unloading; and S: the initial unloading stiffness.

By measuring the mechanical properties of metals with load and depth sensing indentation, Tabor [3] found that though "shallowing" occurred after unloading, the impression shapes kept unchanged only with a larger radius (for a spherical indenter) or a larger included tip angle (for a conical indenter). His observations indicated that the influence of plasticity on the interpretation of elastic unloading data could be dealt with by taking into account the shape of the perturbed surface in the elastic analysis. The shape of the entire unloading curve and the total recovered displacement could be accurately related to the elastic modulus and the size of the contact impression for both spherical and conical indenters. Based on these observations, the effects of non-rigid indenters can be accounted for by defining a reduced modulus, E_r, of the contact, i.e.,

$$\frac{1}{E_r} = \left(\frac{1-\upsilon_i^2}{E_i} \right) + \left(\frac{1-\upsilon_m^2}{E_m} \right) \qquad (3\text{-}5),$$

where E and υ are Young's modulus and Poisson's ratio, and the subscripts i and m indicate the indenter and specimen, respectively.

With the definition of reduced modulus, the indentation with a non-rigid indenter can be treated as a rigid indenter contacting an isotropic elastic half space with modulus E_r. Elastic solution for this case is

$$S = \left. \frac{\partial P}{\partial h} \right|_{elastic} = \frac{2}{\sqrt{\pi}} E_r \sqrt{A} \qquad (3\text{-}6),$$

where S is the experimentally measured contact stiffness of the upper portion of the unloading data and A is the projected contact area. Though it was originally derived for contact between a conical indenter and an elastic isotropic half space, Equation (3-6) applied equally well to spherical and cylindrical indenters [10]. Pharr et al [11]

found that it applied to any indenter that could be described as a body of revolution of a smooth function. For Vickers and Berkovich indenters, finite element analysis by King [12] showed that the deviations from their flat-ended equivalents, the flat-ended punches with square and triangular cross sections, were only about 1.2% and 3.4%, respectively. It is apparent that this equation applies without great error even when the indenter is not a true body of revolution, but sometimes a correction factor β is added to account for the deviation. A triangular type Berkovich indenter has a correction factor β=1.034.

Equation (3-6) gives a method to obtain the elastic modulus of the specimen by interpreting the upper portion of the unloading data in indentation. Theoretically, with this equation and direct measurement of the area of the residual impression formed by the indentation, the elastic modulus may be calculated. However, for nanoindentation in micron and submicron regime, imaging the impressions is both time-consuming and difficult and other means of measurement has to be utilised. In the early 1980s, Pethica et al [13] proposed a simple method to calculate the contact area from the load-displacement curves together with an area function that related the cross-sectional area of the indenter to the distance from its tip. This method was based on the notion that the specimen conformed to the indenter shape to a certain depth at the maximum applied load and the determination of this depth from the *P*-*h* curves allowed the projected contact area to be estimated directly from the area function. Two parameters that could be easily determined from the *P*-*h* curves were the depth at the peak load, h_{max} and the final depth, h_f (see Fig. 3-4). The final depth was found to be able to give a better estimate of the contact area than the depth at the peak load.

Subsequently, Doerner and Nix [14] observed experimentally that, for some materials, the initial portions of the unloading curves were linear, suggesting that the contact area remained constant during initial unloading. This allowed the elastic behaviour of the unloading curve to be modelled by a flat punch indenting an elastic solid. The contact stiffness could be determined from the slope of the initial linear unloading, and for practical purposes, a linear fitting to the upper one third of the unloading curves was used. They also improved the method to find the contact area by extrapolating the initial portion of the unloading curves to zero load and using the extrapolated depth. Their experiments on METGLAS 2826 confirmed that the extrapolated depth did give a better estimate of the contact area than both the depth at the peak load and the final depth. Thus, the elastic modulus of the specimen can be evaluated by Equation (3-6) and the hardness from its definition.

3.3.2 Oliver and Pharr's Method

Oliver and Pharr [10] conducted depth sensing indentations on many materials and found that, even in the initial stages of unloading, the unloading curves were rarely, if ever, linear. Rather, for a variety of tip shapes, unloading curves followed a power law relationship in Equation (3-7) with exponents ranging from about 1.2 to 1.6:

$$P = \alpha (h - h_f)^m \qquad (3\text{-}7),$$

where the constant α, m and h_f were all determined by a least squares fitting procedure to the upper portion of the unloading curve. In addition, using a special dynamic technique to continuously measure the stiffness during indentation, they found that the unloading contact stiffness changed immediately and continuously as the indenter was withdrawn. Their observations suggested that the contact area did not remain constant

even during the initial unloading, and that the flat punch approximation was not an entirely adequate description of real material behaviours. In 1992, Oliver and Pharr [10] developed a new method for interpreting indentation data. It accounted for the curvature in the unloading data and provided a physically justifiable procedure for determining the depth that should be used in conjunction with the indenter shape function to establish the contact area at the peak load. As this method is most extensively used in depth sensing indentations nowadays, a more complete description is given below.

According to the definition of hardness and Equation (3-6), the three key parameters needed to determine hardness and elastic modulus are the peak load (P_{max}), the initial unloading contact stiffness (S_{max}), and the projected contact area, A, at the peak load. P_{max} can be obtained directly from the experiments. S_{max} can be obtained by differentiating Equation (3-7) and evaluating the derivative at the peak load after determining the constants in the equation by a fitting procedure (see Fig. 3-4). The only key parameter to be measured independently is the projected contact area at the peak load.

Sneddon [9] derived an analytical solution for a rigid cone indenting a flat, semi-infinite elastic half space:

$$h = \frac{\pi a}{2\tan\theta} \tag{3-8}$$

and

$$P = \frac{\pi a^2}{2\tan\theta}\frac{E}{1-\upsilon^2} \tag{3-9},$$

where *a* was the radius of the contact circle. Thus the load-depth relationship of a conical indenter into an elastic half space was given by

$$P = \frac{2\tan\theta}{\pi}\frac{E}{1-\upsilon^2}h^2 \qquad (3\text{-}10),$$

and the stiffness of the contact was given by

$$S = \frac{dP}{dh} = \frac{4\tan\theta}{\pi}\frac{E}{1-\upsilon^2}h \qquad (3\text{-}11).$$

In the case of a non-rigid indenter, $E/(1-\upsilon^2)$ was replaced by the reduced modulus E_r. Sneddon [9] also provided a solution for the displacement of the surface surrounding the indenter:

$$h_{el}(r,0) = \frac{2}{\pi}\left[\sin^{-1}\left(\frac{a}{r}\right) - \frac{r}{a} + \frac{\sqrt{r^2-a^2}}{a}\right]h \qquad (r \geq a) \qquad (3\text{-}12),$$

where $h_{el}(r,0)$ was the elastic displacement of the surface surrounding the indenter with a radial distance *r* from the axis of symmetry of the cone.

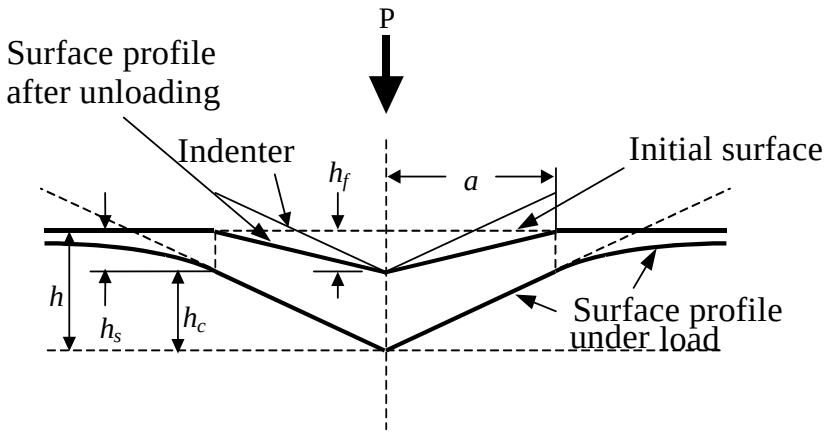

Fig. 3-5 A schematic representation of a section through an indentation showing parameters used in the analysis.

Oliver and Pharr [10] noted that at any time during loading, the total displacement was given by

$$h = h_c + h_s \qquad (3\text{-}13),$$

where h_c was the contact depth, the vertical distance along which the contact was made, and h_s was the displacement of the surface at the perimeter of the contact, as shown in Fig. 3-5. At the peak load, the load and displacement are P_{max} and h_{max}, respectively, and for a conical indenter, the radius of the contact circle is a. At this point, for most materials, h contains both elastic and plastic displacements. Upon unloading, the elastic displacement is recovered, and a residual impression with depth of h_f is left when the load is fully removed.

Oliver and Pharr [10] assumed that Sneddon's solutions applied equally well to indenting a flat surface or a surface with a hardness impression. This assumption was justified basically on the empirical observations that the residual impressions in metals had similar shapes to the indenters used. Particularly, if the geometric parameters describing the effective radius for the spherical indenter and effective tip angle for the cones and indenters of other geometries were adjusted, the mathematical description of the elastic loading and unloading of these perturbed surfaces could be the same as those for the flat surfaces. Thus, the application of Equations (3-10) and (3-11) to the unloading gives

$$P = \frac{2E_r \tan\theta}{\pi}(h - h_f)^2 \qquad (3\text{-}14)$$

and

$$S = \frac{dP}{dh} = 2\left(\frac{2E_r \tan\theta}{\pi}\right)\left(h - h_f\right) \qquad (3\text{-}15).$$

Substitution of r with the contact circle radius a in Equation (3-12) gives the displacement of the surface at the perimeter of contact at the maximum load:

$$h_s = \frac{2}{\pi}\left[\sin^{-1}(1) - 1\right]\left(h_{\max} - h_f\right) = \left(\frac{\pi - 2}{\pi}\right)\left(h_{\max} - h_f\right) \qquad (3\text{-}16).$$

Combination of Equations (3-14) and (3-15) gives

$$\left(h_{\max} - h_r\right) = 2\frac{P_{\max}}{S} \qquad (3\text{-}17).$$

Substituting Equation (3-17) into Equation (3-16) gives

$$h_s = \varepsilon\frac{P_{\max}}{S} \qquad (3\text{-}18),$$

where the geometric constant for a conical indenter is

$$\varepsilon = \frac{2(\pi - 2)}{\pi} = 0.72 \qquad (3\text{-}19).$$

In Equation (3-18), the stiffness S is obtained by analytically differentiating Equation (3-7) and evaluating the derivative at the peak load and displacement.

Similar arguments applied for the flat punch and the paraboloid of revolution give the same equation for h_s but with a different geometric constant. The geometric constants for various indenter tips are shown in Table 3-1.

Indenter type	Flat punch	Sphere	Berkovich	Vickers	Cone
ε value	1	0.75	0.75	0.75	0.72

Table 3-1 ε values for various indenters.

Oliver and Pharr [10] proposed a method for determining area functions that required no imaging based on an assumption that the elastic modulus was independent of indentation depth. They modelled the load frame and the specimen as two springs in series, in which case

$$C = C_s + C_f \qquad (3\text{-}20),$$

where C was the total measured compliance, C_s and C_f were the compliance of the specimen and the load frame, respectively. Since the specimen compliance during elastic contact is given by the inverse of the contact stiffness, S, Equations (3-20) and (3-6) combine to give

$$C = C_f + \frac{\sqrt{\pi}}{2E_r}\frac{1}{\sqrt{A}} \qquad (3\text{-}21).$$

Since the modulus is assumed to be constant, a plot of C versus $A^{-1/2}$ is linear for a given material, and the intercept of the plot is a direct measure of the load frame compliance. The best values of C_f are obtained when C_s, or the second term on the right-hand side of Equation (3-21) is small, i.e., for large indentations. Oliver and Pharr conducted six indentations at different loads in aluminium and obtained initial estimates of C_f and E_r by plotting C versus $A^{-1/2}$ for the two largest indentations in aluminium since in this case, the area function for a perfect Berkovich indenter,

$$A(h_c) = 24.5h_c^2 \qquad (3\text{-}22),$$

could be used to provide a first estimate of the contact area. Using these values, contact areas were computed for all the six indentation sizes by rewriting Equation (3-21) as

$$A = \frac{\pi}{4}\frac{1}{E_r^2}\frac{1}{\left(C - C_f\right)^2} \qquad \text{(3-23)},$$

from which an initial estimation of the area function was made by fitting the area versus contact depth to the relationship:

$$A(h_c) = 24.5h_c^2 + C_1h_c^1 + C_2h_c^{1/2} + C_3h_c^{1/4} ... + C_8h_c^{1/128} \qquad \text{(3-24)},$$

where C_1 through C_8 were constants. In Equation (3-24), the first term described a perfect Berkovich indenter and the rest described the deviations from the perfect shape due to blunting at the tip. Since the exact form of the area function influences the values of frame compliance and reduced modulus, this procedure should be applied and iterated several times using the new area function until convergence is achieved.

Finally, the hardness is computed from its definition at the peak load:

$$H = \frac{P_{\max}}{A} \qquad \text{(3-25)}.$$

The reduced modulus is calculated according to a rewritten form of Equation (3-6):

$$E_r = \frac{\sqrt{\pi}}{2\beta}\frac{S}{\sqrt{A}} \qquad \text{(3-26)},$$

where β is 1.034 for a Berkovich indenter. With the reduced modulus calculated, the Young's modulus of the specimen can be obtained according to

$$\frac{1}{E_r} = \left(\frac{1-\upsilon_i^2}{E_i}\right) + \left(\frac{1-\upsilon_m^2}{E_m}\right) \qquad (3\text{-}5).$$

3.4 Spherical Indentation

Spherical indentation has raised the interests of researchers due to its ability to produce various indentation strains by applying different loads on the indenter. The procedure of interpreting *P-h* curves for spherical indentation was mentioned in the above section. This section will deal with some special characteristics of spherical indentations.

3.4.1 Spherical Indentation Behaviour

A schematic spherical indentation is shown in Fig. 3-6, where *P* is the applied indentation load, *D* is the indenter diameter and *d* is the diameter of contact circle. When plastic deformation occurs, a plastic zone will form in the specimen beneath the spherical indenter.

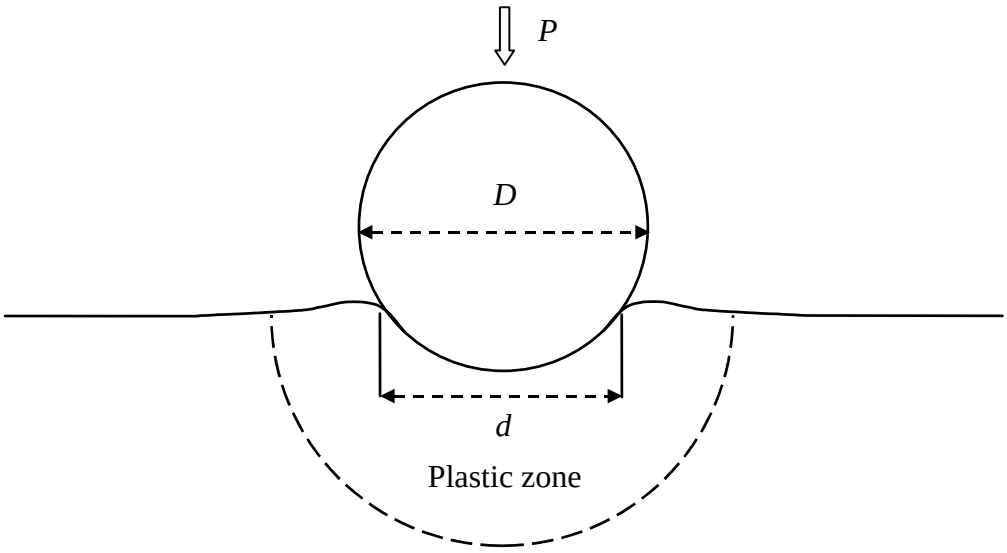

Fig. 3-6 A schematic illustration of spherical indentation. The contact circle has a diameter of *d*.

The deformation of metals under spherical indentation generally experiences three stages distinguished by P_m/Y, where P_m is the projected mean pressure in indentation and Y is the yield stress of metals [3, 15-16].

When P_m/Y <1.1, the deformation is fully elastic and the ratio of P_m to indentation strain d/D is a constant related to reduced modulus E_r, i.e.,

$$P_m = \frac{4E_r}{3\pi}\frac{d}{D} \qquad (3\text{-}27).$$

In this initial elastic stage, the total elastic displacement h was given by Jonhson [17] as

$$h = \frac{d^2}{2D} \qquad (3\text{-}28).$$

As soon as P_m/Y reaches 1.1, plasticity forms at the point of the maximum shear stress, about $0.25d$ beneath the centre of contact circle. This plastic part is surrounded by the outer material deforming elastically. As the indentation load increases at this stage, the mean pressure, p_m, rises and the plastic zone expands. At the same time, for elastic-perfectly plastic materials, the yield stress keeps stable; while for elastic-plastic materials, the yield stress increases to Y_ε corresponding to the current strain ε.

As the indentation load increases further so that P_m/Y or $P_m/Y_\varepsilon \cong 3$, full plasticity is established with the plastic volume expanding to the free surface of specimens and the whole material around the indenter being in a plastic status. From this point on, for elastic-plastic materials, both P_m and Y_ε increase with the ratio of P_m/Y_ε remaining

approximately constant till P_m reaches the ultimate hardness; for elastic-perfectly plastic materials, P_m remains almost constant.

For various metals under indentation with a ball of fixed diameter D, there is an empirical relationship so called Meyer's law:

$$P = Kd^n \qquad (3\text{-}29),$$

where K is a material constant and n is called Meyer index [3]. For fully annealed metals, n is near 2.5 and for fully work-hardened metals it is around 2. Equation (3-29) is valid almost to the indentation size of $d/D \cong 1$, i.e., the penetration depth up to the ball indenter radius. The lower limit for the validity of this equation is about $d/D = 0.1$, the point where fully plasticity is established. At a very low load, metals deform elastically and n increases towards 3. Tabor [3] proposed that the lower limit for Equation (3-29) was dependent upon the hardness of the metal under indentation.

As mentioned above, during the fully plastic stage of spherical indentation on elastic-plastic materials, the yield stress increases with indentation load. However, the yield stress is not constant at every point around the indentation since the amount of deformation or strain varies from point to point. Tabor [3] proposed that, for a fully plastic stage, there existed a representative yield stress, Y_r, which was related to the mean pressure by

$$P_m = cY_r \qquad (3\text{-}30),$$

where c was a constant having a value of around 2.8. Making this assumption, Tabor was concerned with the way in which Y_r depended on the size of the indentation and hence derived a relationship between P_m and the size of indentation.

Tabor [3] expressed the total strain produced in the representative region as a function of indentation size (*d/D*):

$$\varepsilon = \varepsilon_0 + f(d/D) \qquad (3\text{-}31),$$

where ε was the total strain and ε_0 was the initial strain undergone before the indentation in the case of cold-worked materials. Assuming that the yield stress was a single-valued function of the strain, he gave the representative yield stress and mean pressure as

$$Y_r = \phi\{\varepsilon_0 + f(d/D)\} \qquad (3\text{-}32)$$

and

$$P_m = c\phi\{\varepsilon_0 + f(d/D)\} \qquad (3\text{-}33).$$

A convenient method for determining the yield stress of a material is to measure its hardness using a Vickers indenter. The relation between the hardness, the amount of deformation or strain, and the yield stress can be obtained by measuring the Vickers hardness of a metal that is compressed or elongated by various amounts. By this means, the yield stress of a metal undergone spherical indentation can be determined through comparing the Vickers hardness of different points around the residual indentation with that of the same kind of metal that is compressed or elongated. Tabor's [3] indentation experiments at various strains on mild steels indicated that the yield stress of the metal gradually rose in approach to the edge of the indentation, rose rapidly at the edge and then dropped somewhat in approach to the centre of the indentation. He also found that the yield stress at the edge of the indentation might be taken as a representative value for the whole of the deformed material around the indentation

with the constant, *c*, lying between 2.6 and 2.8. He proposed that the indentation stress (i.e., mean pressure) and indentation strain could be used to produce the true stress-true strain curve of uniaxial tensile tests through the following two equations [3, 18]:

$$\sigma_{tensile} = P_m / 2.8 \tag{3-34}$$

and

$$\varepsilon_{tensile} = 0.2\, d / D \tag{3-35}.$$

These two equations, as well as Meyer's law, are effective only in the fully developed plastic contact regime.

Assuming that the yield stress was a simple power function of strain, Tabor [3] deduced the relationship between Meyer's index n and the strain-hardening index x as follows:

$$n = 2 + x \tag{3-36}.$$

During spherical indentation, both the specimen and indenter deform. Tabor [3] pointed out that, to suppress plastic deformation of the indenter, the yield strength of the indenter should be more than 2.5 times that of the specimen. In micro indentations, the spherical indenter is usually made of polished diamond due to its high modulus and hardness. Indenter geometry is a very important factor among the uncertainty sources in micro indentations and nanoindentations because at small penetrations the indenter crosssection can be far away from a perfect shape. In nanoindentations, though the projected contact area could be corrected through area function by use of a standard material, usually fused silica, the curvature radius of contact may change with the

penetration depth and so the nominal indenter radius is used to calculate the indentation strain.

3.4.2 Stress Field of Spherical Indentation

The elastic stress field arising from various indenters, such as a sphere, cylinder and pyramid, can be well defined based on the solution of the contact between two elastic bodies, which was first studied by Hertz [2] in 1881 before his more well-known work on electricity. To define a framework that provides a formulated mathematical treatment of the problem, He proposed certain boundary conditions, namely:

a) The displacements and stresses must satisfy the differential equations of equilibrium for elastic bodies and that the stresses vanish at a great distance from the contact surface;

b) The bodies are in frictionless contact;

c) In the surface of the bodies, the normal pressure is zero outside, and equal and opposite inside the circle of contact;

d) The distance between the surfaces of the two bodies is zero inside, and greater than zero outside the contact circle;

e) The integral of the pressure distribution within the circle of contact with respect to the area of the circle of contact gives the force acting between the two bodies.

Hertz [2] found that an ellipsoidal distribution of pressure would satisfy the boundary conditions and that for the case of a spherical indenter on a semi-infinite half-space, the required distribution of normal pressure was

$$\frac{\sigma_Z}{P_m} = -\frac{3}{2}(1-\frac{r^2}{a^2})^{1/2} \quad (r \le a) \qquad (3\text{-}37),$$

where σ_Z was the stress normal to the semi-infinite half-space, P_m was the mean pressure, r was the distance from load axis and a was the contact circle radius.

In 1904, Huber [19] first calculated in detail the stress field associated with spherical indentation on a flat surface. Later, the integral transform method of Sneddon [20] was applied to normal pressure distribution under a variety of axis-symmetric indenters. The widely used solutions to practical applications were provided by Johnson [17]. The solutions of elastic stress field for spherical indentation are summarized below.

According to Equation (3-37), σ_Z is at its maximum at the centre of contact and is zero at the contact circle edge. Outside the contact circle is a free surface with normal stress of zero.

In the specimen surface, the radial stress σ_r is defined by:

$$\frac{\sigma_r}{P_m} = \frac{1-2\upsilon}{2}\frac{a^2}{r^2}\left[1-\left(1-\frac{r^2}{a^2}\right)^{3/2}\right]-\frac{3}{2}\left(1-\frac{r^2}{a^2}\right)^{1/2} \quad (r \le a) \quad (3\text{-}38)$$

and

$$\frac{\sigma_r}{P_m} = \frac{1-2\upsilon}{2}\frac{a^2}{r^2} \qquad (r \ge a) \qquad (3\text{-}39).$$

In the above formulae, υ is the Poisson ratio of the specimen. The hoop stress σ_θ is always a principal stress and, outside the contact circle, is equal to the radial stress in magnitude but with opposite mark, i.e.,

$$\sigma_\theta = -\sigma_r \qquad (r>a) \qquad (3\text{-}40).$$

Within the bulk of the specimen, the stresses are defined by the following formulae:

$$\frac{\sigma_r}{P_m} = \frac{3}{2}\left\{\begin{array}{l}\dfrac{1-2\upsilon}{3}\dfrac{a^2}{r^2}\left[1-\left(\dfrac{z}{u^{1/2}}\right)^3\right]+\left(\dfrac{z}{u^{1/2}}\right)^3\dfrac{a^2u}{u^2+a^2z^2}+ \\ \dfrac{z}{u^{1/2}}\left[u\dfrac{1-\upsilon}{a^2+u}+(1+\upsilon)\dfrac{u^{1/2}}{a}\tan^{-1}\left(\dfrac{a}{u^{1/2}}\right)-2\right]\end{array}\right\} \qquad (3\text{-}41),$$

$$\frac{\sigma_\theta}{P_m} = -\frac{3}{2}\left\{\begin{array}{l}\dfrac{1-2\upsilon}{3}\dfrac{a^2}{r^2}\left[1-\left(\dfrac{z}{u^{1/2}}\right)^3\right]+ \\ \dfrac{z}{u^{1/2}}\left[2\upsilon+u\dfrac{1-\upsilon}{a^2+u}-(1+\upsilon)\dfrac{u^{1/2}}{a}\tan^{-1}\left(\dfrac{a}{u^{1/2}}\right)\right]\end{array}\right\} \qquad (3\text{-}42),$$

$$\frac{\sigma_z}{P_m} = -\frac{3}{2}\left(\frac{z}{u^{1/2}}\right)^3\left(\frac{a^2u}{u^2+a^2z^2}\right) \qquad (3\text{-}43),$$

and

$$\frac{\tau_{rz}}{P_m} = -\frac{3}{2}\left(\frac{rz^2}{u^2+a^2z^2}\right)\left(\frac{a^2u^{1/2}}{a^2+u}\right) \qquad (3\text{-}44),$$

where z is the vertical distance from the specimen surface, τ_{rz} is the shear stress and u is defined as

$$u = \frac{1}{2}\left\{\left(r^2+z^2-a^2\right)+\left[\left(r^2+z^2-a^2\right)^2+4a^2z^2\right]^{1/2}\right\} \qquad (3\text{-}45).$$

In the specimen, the principal stresses and maximum shear stress are defined by

$$\sigma_{1,3} = \frac{\sigma_r+\sigma_z}{2} \pm \sqrt{\left(\frac{\sigma_r-\sigma_z}{2}\right)^2+{\sigma_{rz}}^2} \qquad (3\text{-}46),$$

$$\sigma_2 = \sigma_\theta \qquad (3\text{-}47),$$

and

$$\tau_{\max} = \frac{1}{2}(\sigma_1 - \sigma_3) \qquad (3\text{-}48).$$

The angle α between σ_1 and the *r* axis is defined by

$$\tan\alpha = -\frac{\sigma_r - \sigma_z}{2\tau_{rz}} \pm \left[\left(\frac{\sigma_r - \sigma_z}{2\tau_{rz}}\right)^2 + 1\right]^{1/2} \qquad (3\text{-}49).$$

On the surface, the principal stresses σ_1, σ_2 and σ_3 become σ_r, σ_θ and σ_z, respectively. Inside the contact circle, all the principal stresses are compressive and $\sigma_1 > \sigma_2 > \sigma_3$ holds in most of the contact area. Outside the contact circle, however, the stress field is quite different. The first principal stress, σ_1, becomes tensile and the second principal stress, σ_2, remains compressive, of which the magnitudes are the same and decrease with the radial distance. The radial stress, σ_r, is mainly responsible for the crack initiation and the hoop stress, σ_θ, expands the crack initiation into a ring crack. The third principal stress, σ_3, drops to zero, indicating that the stress in the surface outside the contact circle is a pure shear stress 45° to the radial direction (Fig. 3-7). Since both the radial stress and hoop stress change their directions when the reference point moves along the trajectories of the shear stresses, the trajectories of the pure shear stresses in the specimen surface are not straight, but in spiral shapes.

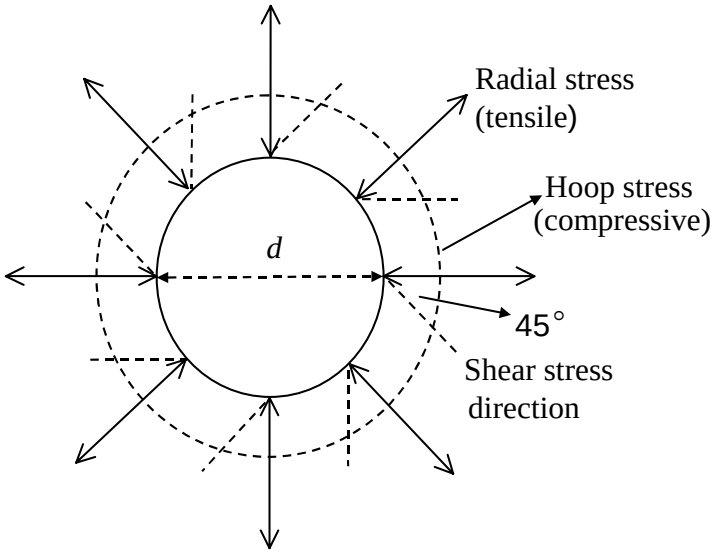

Fig. 3-7 Pure shear stresses on the specimen surface during elastic spherical indentation.

When plasticity presents beneath the indenter, analytical treatments of the indentation stress field can be very complex and therefore finite-element method is used for substitution. The presence of the plastic zone significantly changes the near-field indentation stresses, while the far-field stresses are little changed from the elastic case [17]. In the near field (r<2a), generally the magnitudes of the maximum principal stresses shift outwards, away from the contact center, when compared with the elastic case, indicating an outward shift in upward pressure distribution or a more uniformly distributed contact pressure.

The stress distribution in the surface for the elastic-plastic case is also different from that for elastic indentation. Within the contact zone near the edge of contact circle, all stresses increase in magnitude. Finite element simulation results for spherical indentation on glass-ceramic materials indicated that, outside the contact zone, the principal stresses changed from compressive status to tensile status at r/a ~ 1.3 and after that they dropped to zero [21]. It should be noted that, outside the contact circle, the radial stress and the hoop stress are not equivalent in magnitude, which is different from the case of elastic indentation. When they are compressive, the radial stress is

slightly smaller than the hoop stress, but when they are tensile, the radial stress is much larger than the hoop stress before they drop to zero.

3.5 Uncertainties in Indentation

During indentation, some uncertainties should be taken into account. These uncertainties mainly include pile-up and sink-in in specimen, indenter geometry, thermal drift, machine compliance and initial penetration depth [4, 22], of which the latter four are related to measuring equipment and are important in nanoindentation. Indentation size effect also plays a role in low load nanoindentations. These uncertainties are briefly discussed below.

3.5.1 Pile-up and Sink-in

If neither pile-up nor sink-in occurs during indentations, for an ideal Berkovich (or Vickers) indenter the projected contact area is the indenter crosssectional area, only related to the contact depth according to

$$A(h_c) = 24.5h_c^2 \qquad (3\text{-}22).$$

In this case, the materials around the indenter side and indenter corner are in a same level. However, when pile-up occurs during indentation, the material beside the indenter side is higher than the material contacting the indenter corner, of which the height is considered as contact depth h_c. Thus the actual contact area is more than that obtained according to Equation (3-22) and thus the Young's modulus and hardness are overestimated if Equation (3-22) is used for calculation. In the case of sink-in, the material beside indenter side is lower than the material around indenter corner, which

can cause the Young's modulus and hardness to be underestimated. These two cases are shown in Fig. 3-8.

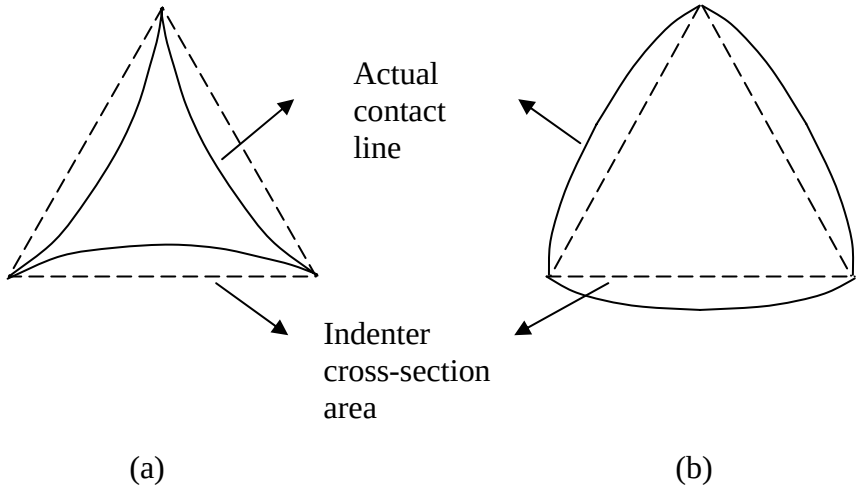

Fig. 3-8 Top view of the contact area in situations of (a) sink-in and (b) pile-up.

The behaviour of pile-up and sink-in depends on the ratio of the Young's modulus to the yield strength, E/Y, and the strain hardening properties of the material. Pile-up is often observed in non-strain hardening materials with a high E/Y, such as strain-hardened metals. Sink-in is often pronounced for strain hardening materials, such as annealed metals, and non-strain hardening materials with a low E/Y, such as ceramics.

3.5.2 Indenter Geometry

In interpreting the nanoindentation testing, the contact area at penetration depth, h_p, equivalent to h_c, is obtained from the geometry of an ideal indenter. However, in practice the indenter is impossible to be ideal and it is necessary to apply a correction factor to determine the real area of contact. For a given h_p, the actual contact area is A and the ideal one is A_i. The correction factor A/A_i is illustrated in Fig. 3-9.

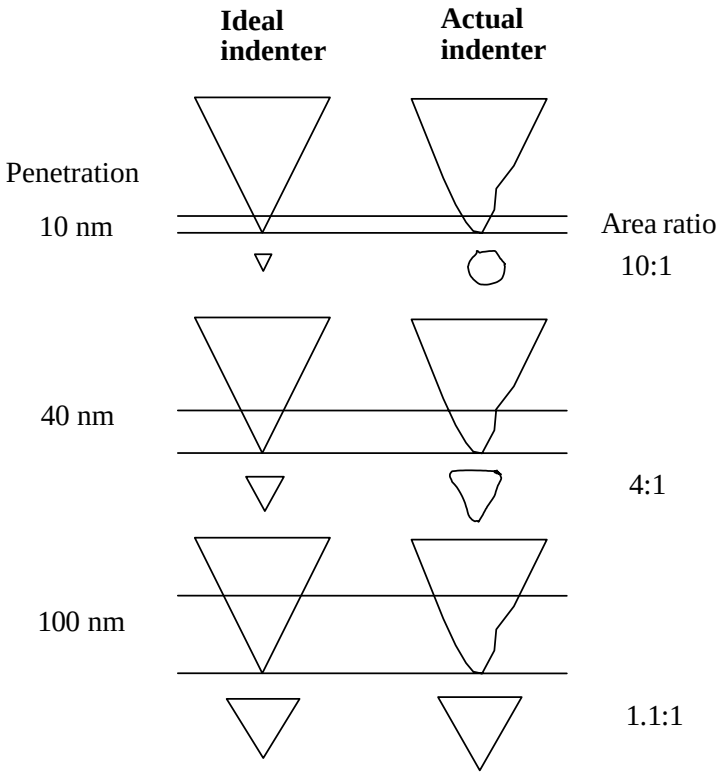

Fig. 3-9 Relationship between area correction factor and the penetration depth. The actual contact area approaches the ideal contact area as the penetration depth increases [23].

The correction factor can be determined from independent measurements of the indenter geometry using either an Atomic Force Microscope (AFM) or Scanning Electronic Microscope (SEM). However, it is inconvenient to measure the indenter geometry at various penetration depths h_p. Nowadays a regular practice is to determine area functions indirectly by performing a series of indentations at different maximum load on reference specimens whose Young's modulus and Poisson's ratio are known. Values of A and h_p for each test on the reference material provide the data for an area function lookup or calibration table. It is often convenient to express the area function as a ratio A/A_i.

3.5.3 Creep and Thermal Drift

During an indentation, when the load is held constant, the depth may change with time. There are two reasons for this drift behaviour. One is the creep in the material as a result of plastic flow. When the creep occurs, the depth reading keeps increasing at a constant load, which is usually measured at the maximum load hold process. The other reason for the depth change is thermal drift, the change in dimensions of the instrument due to thermal expansion or contraction. Thermal drift can arise from changes in the temperature of the test environment or from heat generating components within the indentation instrument itself. Though thermal drift is small compared to creep, it cannot be ignored in nanoindentation. The usual practice to correct for thermal drift is to allow a hold series of data points to be accumulated at the end of the unloading from maximum load. The thermal drift rate is then calculated and applied to all the depth readings.

3.5.4 Machine Compliance

Due to the reaction force during indentation, both the specimen and the instrument deform. The displacements of both instrument and specimen are logged by the depth measuring system and interpreted as the penetration into the specimen, leading to an overestimated penetration depth.

The deflection of the instrument divided by the load is defined as C_f, the compliance of the loading instrument. Besides the elastic deformation of the specimen, C_f also contributes to the unloading stiffness, dP/dh. Taking the instrument compliance into account, the total compliance measured by the instrument is

$$\frac{dh}{dP} = \frac{1}{S} + C_f \qquad (3\text{-}50),$$

where S is specimen stiffness.

The main method of obtaining C_f is to plot dh/dP versus $1/\sqrt{A}$ obtained for elastic unloading into an elastic-plastic material for a range of maximum indentation depths. The plot should be linear with a slope proportional to $1/E_r$ and the intercept gives the instrument compliance directly. As the compliance obtained in this way depends on the area function of the indenter, an iterative procedure is necessary to arrive at a converged value. In routine data analysis of indentation tests, the compliance of the instrument may be subtracted from experimental values of dh/dP before calculating E_r.

3.5.5 Initial Penetration Depth

At the beginning of nanoindentation, the indenter contacts the specimen with a small load so that the instrument can detect the specimen surface. This small load is referred to as initial contact force and upon this force the depth reading is recognized as zero. The initial contact force is usually made to be as small as possible. However, no matter how small the initial contact force is made, it will create a corresponding non-zero initial penetration depth h_i. Thus, all subsequent depth readings will be in error by this small initial penetration depth. In analysis, h_i has to be added to all depth readings, h, to correct for the initial displacement of the specimen. The initial penetration depth is usually obtained by fitting the first several load-depth data points into a curve and the intercept with axes of depth is taken as h_i.

3.5.6 Indentation Size Effect

It is often observed that for sharp indenters such as Berkovich and Vickers, hardness and/or modulus rises as the penetration depth decreases. Some of the observed effects indeed reflect the mechanical properties of specimen surface that are different from those of the bulk. Such differences may arise from the very thin oxide films on the surface or the presence of residual stresses and strain hardening due to specimen preparation. Friction between the indenter and specimen is also found to attribute to size effect. However, even if these effects are minimized, it is still observed that an indentation size effect exists for some materials, such as crystalline solids, which are nominally isotropic.

In materials exhibiting an indentation size effect, the conditions for plastic flow are assumed to depend not only on the strain, but also on the strain gradient. For a sharp indenter, the strain produced is a constant and thus the strain gradient is large when penetration depth decreases. It is proposed that strain gradient introduces additional dislocations, which in turn increases the hardness. For polycrystalline metals the size effect can be modelled as follows [4]:

$$\frac{H}{H_0} = \sqrt{1 + \frac{h^*}{h}} \qquad \text{(3-51)},$$

where H and H_0 are the hardness with and without size effect, h is indentation depth and h^* is a material constant.

Besides the factors discussed above, other factors that affect nanoindentation tests include specimen surface roughness, indenter tip rounding, residual stress status and defects produced in specimen preparation.

3.6 Depth-sensing Indentation Systems

3.6.1 Ultra Micro Indentation System (UMIS)

UMIS was developed in the mid 1980s at the National Measurement Laboratory (NML) of the Commonwealth Scientific and Industrial Research Organisation (CSIRO) in Australia. It is a sub-micrometer to micrometer scale hardness testing instrument that uses both pyramidal and spherical diamond indenters with automatic analysis for experimental data. The UMIS is a "force-driven static measuring" indentation instrument for investigating the mechanical properties of materials [22]. It is "force-driven" in the sense that the indenter is driven into the surface until a resistance equal to a set force is met. It is "static measuring" in the sense that penetration is measured under conditions of force equilibrium at each of a series of force steps.

The main components of the UMIS are: base, column and enclosure; electronics and control; positioning stage; optical microscope; indenters; and accessories.

The base provides both thermal and mechanical stability to the instrument. It is a seismic mass, which, together with the damped mounting springs, reduces the effect of mechanical vibration from the surroundings. The column contains the most sensitive parts of the UMIS, such as the electronics and control parts. The enclosure is designed to reduce to a minimum thermal and electrical interference to the UMIS instrument. It is double-lined with insulation and also contains a special electromagnetic shielding layer. The electronics and control parts receive signals from a computer, measure the force and depth and send back the information to the computer. The positioning stage makes the specimen positioned under the optical microscope and can transport the specimen to the position of indentation.

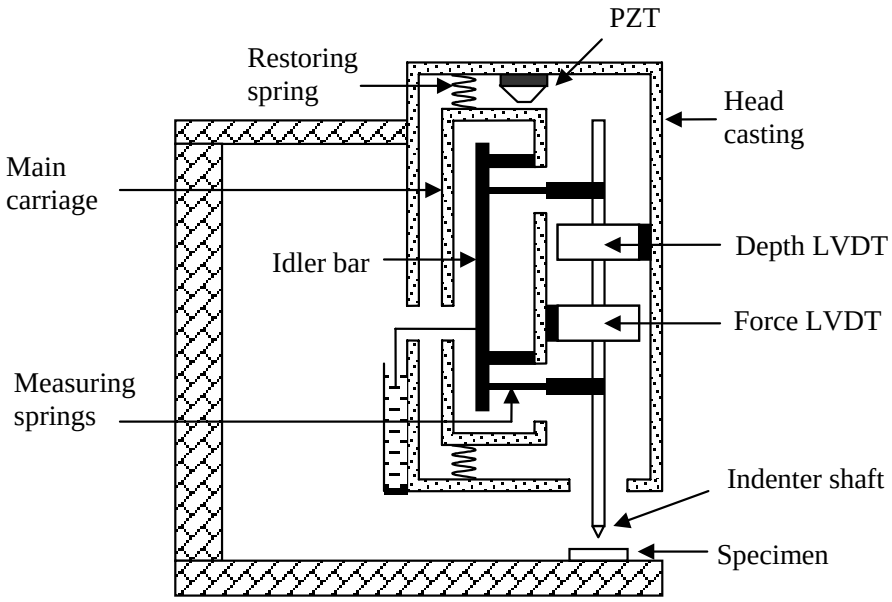

Fig. 3-10 Schematic figure of UMIS [23].

The principle of operation is shown in Fig. 3-10. The indenter is mounted on a shaft that is attached to a carriage by a series of carefully machined leaf springs. The carriage is driven by the expansion of a piezo-electric device and when the indenter contacts the specimen, the springs deflect. This deflection is measured by the Force Linear Variable Differential Transformer (LVDT). The measured spring deflection is proportional to the load and is used in a feedback loop to maintain the indenting force at the desired level. This force is maintained regardless of the amount of indenter penetration into the surface of the specimen. The feedback system ensures precise control over the application of the force. A separate Depth LVDT measures the displacement of the indenter shaft relative to the carriage. The Depth LVDT provides a voltage signal that is linearly proportional to the displacement from its zero position.

A standard UMIS has measurement range A and range B. The maximum penetration and force for range B are ten times larger than those for range A. The specifications for the often used range A are shown in table 3-2.

Measuring System	Specifications (range A)
Penetration ranges	0-2 μm
Displacement resolution	0.05 nm
Measurable resolution	< 0.1 nm
Maximum total force ranges	50 mN
Force resolution	0.75 μN
Internal noise uncertainty	< 0.5 μN
Minimum contact force	<5.0 μN
Number of loading steps	Selectable from 1 to 200

Table 3-2 UMIS specifications (force and depth) [22].

A UMIS indentation test involves quite a number of parameters, which contain the descriptive information about the test, the procedure control, timing and analysis. Some important parameters are briefed below.

The UMIS indentation can be conducted in two control modes: force control and depth control. In the force control mode, the desired maximum force is specified and the UMIS attempts to apply this force incrementally and then records the resulting depth of penetration. The force can be applied in either linear or square root progression. The linear progression provides an evenly spaced distribution of force, and the square root progression creates a greater number of force increments during the initial application of load compared with near the maximum force. The advantage of the square root progression is that the resulting depth measurements will be nearly linearly spaced. In the depth control mode, the maximum depth of indentation rather than the maximum force is specified. However, the actual instrument works in a force control mode, with the depth control achieved by applying small increments of force and reading the resulting depth. The load increments to use in this method of operation are set in the timing part. The number of decrements for the unloading process can also be specified but it is usually set to be the same as that of increments.

Time related parameters also play an important role in UMIS indentation tests. A time delay can be set before any test starts. This is very useful when a test is to be performed at late night when there are the minimum of mechanical disturbances and other uncertainties. The rate of penetration at each force increment can be adjusted through rate control. There is a dwell time at each load increment and decrement to allow the load and depth readings to stabilise before being taken. There is also a hold time at the maximum force and the final unload. The hold at the maximum load is usually for testing of the time-dependent properties of a material (or creep), and the final unload hold is usually for thermal drift correction in the data analyse.

3.6.2 Nano Indenter XP

Nano Indenter XP is a kind of nanoindentation system that is developed by MTS Systems Corporation (MTS, USA). Its main components include indentation head assembly, Motorized sample manipulation table, Optical imaging system, data acquisition and control system, Vibration isolation table and Environmental isolation enclosure. The physical mechanisms involved in this machine are briefed below.

Sample positioning is carried out when observing the sample surface through an optical microscope. Then the sample is automatically translated to the indenter and tests are performed at the desired locations. Theoretical resolution for sample positioning is 45 nm with a real accuracy of about 1.5 μm [23].

Different from UMIS in which the indenter is driven by a piezo-electric device, Nano Indenter XP imposes the desired force on the indenter by passing current through a coil that sits within a circular magnet. The force imposed on the indenter shaft in this way, with theoretical resolution of 50 nN, is directly proportional to the current passed through the coil [23]. Since the force on the indenter is imposed electromagnetically, the machine is not suitable for magnetic samples, which may interfere with the

operation of the instrument. Although the machine may be operated under displacement control, it its fundamentally load controlled, which is similar to the case of UMIS. The distinction between these two methods becomes important only when the test sample exhibits some kind of sudden failure, upon which the displacement increases suddenly at a given applied load.

The displacement sensing system consists of a capacitive arrangement of three circular plates. The two outside plates are fixed and have holes in the center just large enough to accommodate the indenter shaft. The center plate is fixed to the indenter shaft and is free to move vertically between the two outside plates. The position of the indenter column within the gap is determined by observing the difference in voltage between the center plate and either of the two outside plates. The theoretical displacement resolution of this plate-and-indenter assembly is less than 0.01 nm [23].

Nano Indenter XP provides various control modes of the indentation experiment. Users are able to control the rates and limits for constant loading rate, constant displacement rate, or constant strain rate tests. During nanoindentation experiments, the strain rate is defined as $\frac{1}{h}\frac{dh}{dt}$, where h is the displacement of indenter and t is time [4]. The control software of Nano Indenter XP also provides flexible programming of the indentation experiment process. For example, users can cycle the load until any specified event-whether it is number of cycles, maximum displacement, minimum average displacement rate, or specified contact stiffness-occurs.

Reference:

1. O"Neill, H., *Hardness Measurement of Metals and Alloys*, The Thanet Press, Margate (1967).

2. Hertz, H., *Mathematik*, **92**, 156 (1881).

3. Tabor, D., *The Hardness of Metals*, Oxford University Press, London (1951).

4. Fischer-Cripps, A. C., *Nanoindentation*, Springer-Verlag New York, Inc., New York (2002).

5. Boussinesq, J., *Application des Potentiels a l"Etude de l"Equilibre et du Mouvement des Solides Elastiques*. Gauthier-Villars, Paris (1885).

6. Love, A. E. H., *The Quarterly Journal of Mathematics*, **10**, 161 (1939).

7. Sneddon, I. N., *Proceedings of the Cambridge Philosophical Society*, **42**, 29 (1946).

8. Sneddon, I. N., *Proceedings of the Cambridge Philosophical Society*, **44**, 492 (1948).

9. Sneddon, I. N., *International Journal of Engineering Science*, **3**, 47 (1965).

10. Oliver, W. C. and Pharr, G. M., *Journal of Materials Research*, **7**, 1564 (1992).

11. Pharr, G. M., Oliver, W. C. and Brotzen, F. R., *Journal of Materials Research*, **7**, 613 (1992).

12. King, R. B., *International Journal of Solids and Structures*, **23**, 1657 (1987).

13. Pethica, J. B., Hutchings, R. and Oliver, W. C., *Philosophical Magazine A*, **48**, 593 (1983).

14. Doerner, M. F. and Nix, W. D., *Journal of Materials Research*, **1**, 601 (1986).

15. Field, J. S. and Swain, M. V., *Journal of Materials Research*, **10**, 101 (1995).

16. Fischer-Cripps, A. C., *Introduction to Contact Mechanics*, Springer-Verlag New York, Inc., New York (2000).

17. Johnson, K. L., *Contact Mechanics*, Cambridge University Press, Cambridge (1985).

18. Herbert, E. G., Pharr, G. M., Oliver, W. C., Lucas, B. N. and Hay, J. L., *Thin Solid Films*, **398-399**, 331 (2001).

19. Huber, M. T., *Annalen der Physik*, **14**, 153 (1904).

20. Sneddon, I. N., *Fourier Transforms*, McGraw-Hill, New York (1951).

21. Care, G. and Fischer-Cripps, A.C., *Journal of Materials Science*, **32**, 5653 (1997).

22. Fischer-Cripps, A. C., *Winumis Software User Manual*, CSIRO, Lindfield (2001).

23. MTS Systems Corporation, *TestWorks® 4 Software for Nanoindentation Systems*, MTS Systems Corporation, Oak Ridge (2001)

Chapter 4 Experiments

4.1 Specimen Preparation

Alloy $Zr_{52.5}Ti_5Cu_{17.9}Ni_{14.6}Al_{10}$ (at%) was prepared by arc melting of the pure elements Zr (99.99%), Ti (99.95%), Cu (99.99%), Ni (99.98%) and Al (99.9%) under a Ti-gettered Ar atmosphere. The glass ingots were obtained by sucking the re-melted alloy into the cavity of a water-cooled copper mould under a Ti-gettered Ar atmosphere. The resulting ingot dimensions are 1.5×5×30 mm^3. After the samples were confirmed by XRD to be amorphous, they were mechanically polished to mirror smooth before indentation experiments were performed. During mechanical polishing, cooling agent and low polishing speed were employed to keep temperature far below T_g , ruling out the possibility of glass transition and nanocrystallization during specimen preparation.

4.2 Preliminary Material Characterization

A General Area Detector Diffraction System (GADDS, Bruker AXS Inc., USA) is used at a 40 KV voltage and 20 mA current for structural characterisation of metallic glass $Zr_{52.5}Ti_5Cu_{17.9}Ni_{14.6}Al_{10}$. The GADDS has an area detector, which is different from conventional detector because of its ability to collect the diffraction data beyond the diffraction plane. Thus the Debye rings shown on the area detector are arcs, not short straight lines (refer to Fig. 4-1). The diffraction intensity versus 2θ from 20° to 90° is obtained by integration of the data, where θ is Bragg angle. The target material is Cu and the x-ray wavelength is Kα radiation. The GADDS uses a laser beam to position the sample.

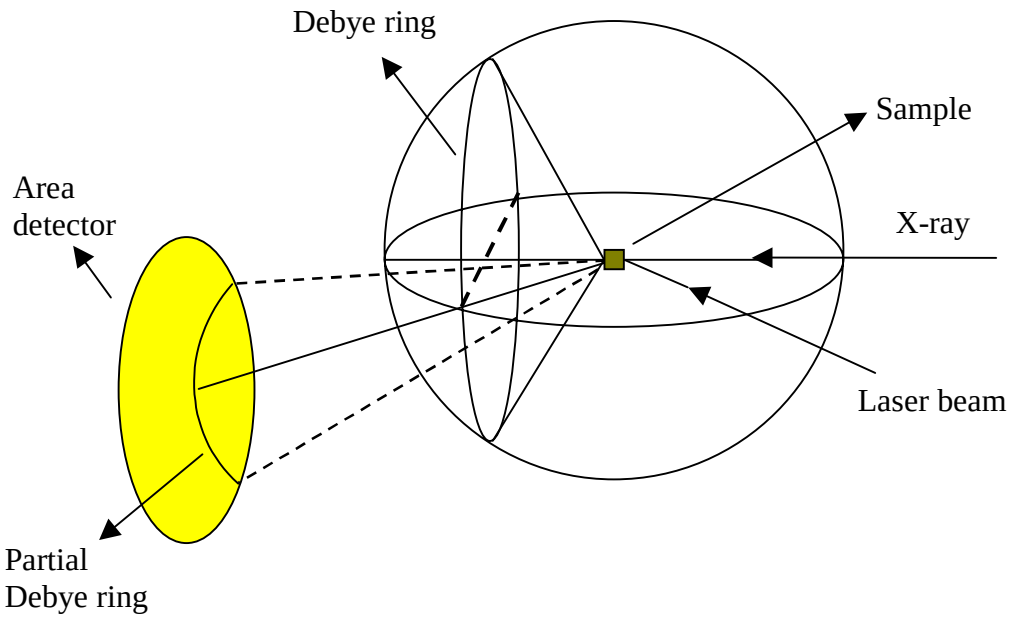

Fig. 4-1 Schematic figure of XRD. The Debye ring on the area detector is an arc, which records the data beyond the diffraction plane. The sample is located at the crossing point between the x-ray and the laser beam.

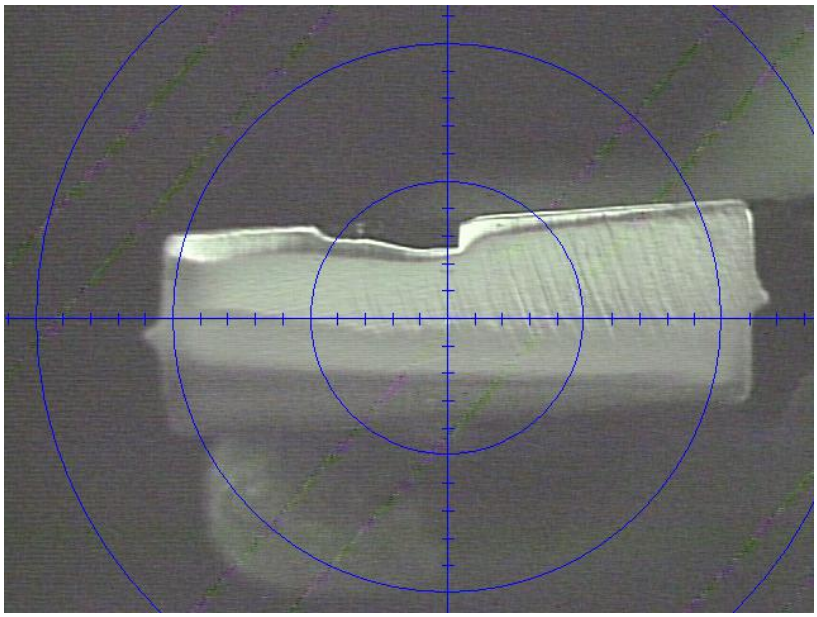

Fig. 4-2 Sample positioning in XRD. The white rectangle in the figure is the cross section of the sample. When the laser beam incidence point on the sample is at the centre of video system, the sample is correctly positioned.

In the XRD settings, the centre of Ewald Sphere is located at the crossing point of the x-ray and a laser beam. This crossing point is also on the optical shaft of a video

system. When the sample is adjusted so that the laser beam incidence point on the sample is located at the cross of the video (refer to Fig. 4-2), this incidence point is also the exact incidence point of the x-ray and the sample is correctly positioned. Once the sample is correctly positioned, the incidence point does not move with the rotation of sample.

4.3 Indentation

Three indentation machines were used to conduct indentations on metallic glass $Zr_{52.5}Ti_5Cu_{17.9}Ni_{14.6}Al_{10}$: Microforce Tester (Instron 8848, USA), UMIS-2000 (CSIRO, Australia) and Nano Indenter XP (MTS, USA). Details of UMIS and Nano Indenter XP were provided in Chapter 3 and thus a brief introduction to Microforce tester is given here.

With different accessories mounted, Microforce Tester can be used to conduct various kinds of tests, including compression, tension, bending and indentation. The machine is driven by hydraulic pressure with the maximum force of 1 KN. The applied loads are recorded by four load cells with different load ranges: 5 N, 10 N, 100 N and 1 KN. Though this machine can conduct depth-sensing indentations, we adopted the conventional hardness testing method due to the facts that the indentation depth was very small compared to the depth range of the machine and that the residual indentation impressions were large enough to be precisely measured by optical microscope. Spherical indentations were performed on the metallic glass by using a spherical diamond indenter tip mounted on the Microforce Tester. Diamond has Young's modulus around 1000 GPa and hardness around 100 GPa, much higher than those of metallic glasses, and thus can be treated as a rigid indenter during indentation on metallic glasses. The indenter was confirmed to possess ideal spherical shape with

200 μm in radius in the range of indentation experiments (Fig. 4-3). The indentations were conducted under load control mode with load range of from 10 N to 240 N at a nominal displacement rate of 0.1 mm/min.

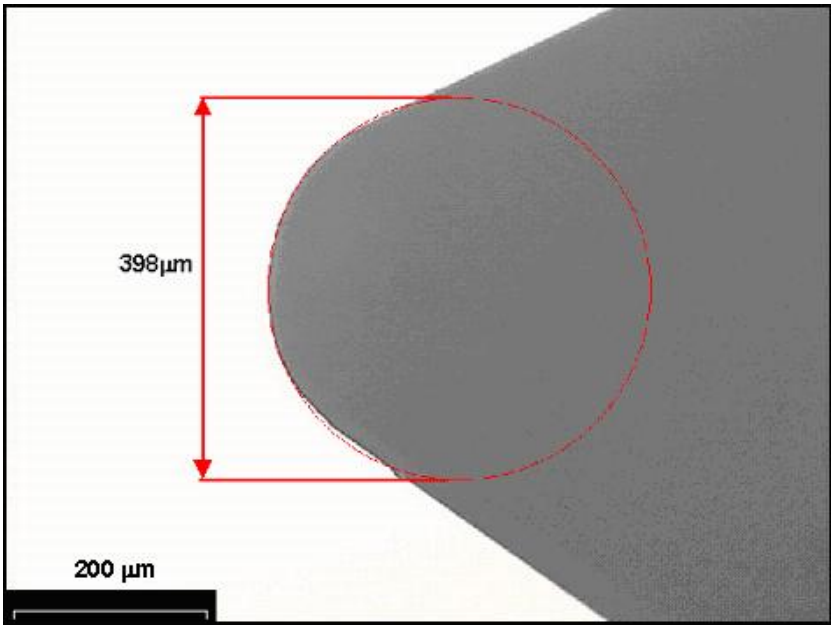

Fig. 4-3 Shape of the spherical diamond indenter tip. When the depth is less than 50 μm or the contact circle diameter is less than 260 μm, the diamond tip can be treated as an ideal ball indenter. (Optical image by Olympus BX60.)

To investigate the effect of the residual spherical indentation impression on the mechanical properties of the metallic glass, we performed nanoindentations on the material around the spherical impression by using Berkovich diamond indenter tip on UMIS-2000 as a probe. We chose an impression produced by a large load (230 N) to be studied so that the material around the impression achieved a fully plastic stage. Nanoindentations were conducted on the free surface radially outwards from 20 μm to 240 μm away from the edge of spherical indentation impression with spacing of 20 μm. The nanoindentations were set with the maximum load of 40 mN and 30 load increment steps under square root progression load control mode.

The effect of the residual spherical indentation impression was further investigated by using Nano Indenter XP. A series of Berkovich nanoindentations at the load of 40 mN and loading rate of 0.02 mN/s were performed around a residual spherical impression produced by 260 N. Using nanoindentations at this low loading rate, we were able to study the plastic deformation of the metallic glass in more details.

4.4 Compression

To study the relationship between the hardness and yield strength of the metallic glass, we performed compressive tests to obtain the yield strength. The samples were machined to the dimensions of $1.5\times1.5\times3$ mm^3, with two ends mechanically polished to be parallel. The experiments were conducted using Servohydraulic Testing Machine (Instron 8872, USA), which was driven by hydraulic pressure with capacity of 25 KN, at the strain rate of 10^{-4} s^{-1}. The built-in displacement LVDT is not suitable for small specimens, with the measured displacement more than the actual displacement of specimens. In view of this, we only used the measured stress for study.

4.5 Surface Morphology Characterization

The sample morphology after indentation and compressive tests was examined by optical microscope (Olympus BX60, Japan), SEM (JEOL 5600 and JEOL 6700F, Japan) and AFM (DI multimode, Veeco, USA). Such examinations provided further information about mechanical deformation of metallic glasses.

Chapter 5 Results and Discussion

5.1 Material Characterization

The structures of the as-cast specimens were characterized by using of XRD. XRD experiments were conducted on different spots on the cross section of samples, especially the centre where the cooling rate is low and crystallization is more likely to take place. The typical XRD pattern of as-cast alloy (Fig. 5-1) shows two intensity humps. Researches [1-2] indicate that, when partial amorphousness or crystalline exists in metallic glass, small diffraction peaks generally appear on top of the humps. In our case, no Bragg peaks are found on the humps, indicating no evidence of crystalline structure in the samples.

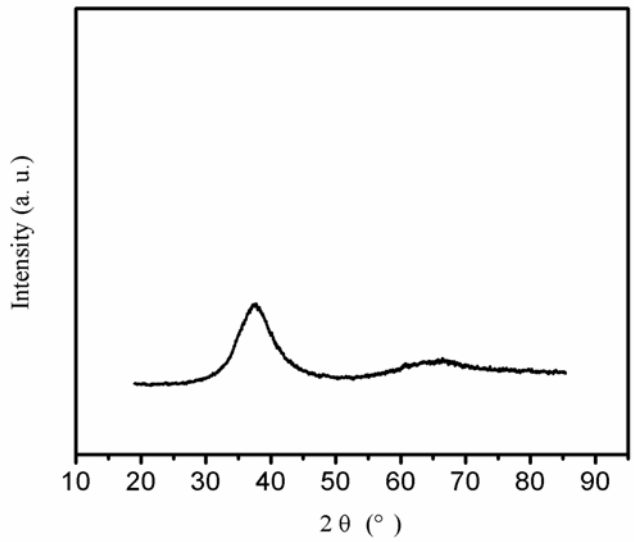

Fig. 5-1 Typical XRD pattern for as-cast BMG $Zr_{52.5}Ti_5Cu_{17.9}Ni_{14.6}Al_{10}$.

5.2 Spherical Indentation Behaviour

One characteristic of spherical indentation is its ability to characterize the mechanical behaviour of materials upon different indentation strain status. To

characterize the spherical indentation behaviour of the metallic glass, a spherical diamond indenter tip with radius of 200 μm was pressed into the specimen at loads from 10 N to 240 N.

The mean pressure during the spherical indentation is obtained from the applied load divided by the projected contact area. As shown in Fig. 5-2, the mean pressure increases with increasing load until it reaches about 5.5 GPa at the load of 160 N. After that, the mean pressure remains constant upon further increment in the indentation loads. Due to the lack of crystalline structure and dislocation, metallic glasses are perfectly plastic and unable to strain harden. During compressive tests on metallic glasses, some researchers found that after the elastic limit of metallic glasses, the stress keeps constant while compressive strain increases [3]. In spherical indentation, perfect plasticity is demonstrated by the constant mean pressure upon increasing load. In this case, perfect plasticity is achieved upon loads larger than 160 N. When the applied load is less than 160 N, the mean pressure increases with the load applied, indicating that the metallic glass is at a transition stage from elastic deformation to plastic deformation. The plot does not show the fully elastic indentation part because the material will recover to its original shape upon the load removal and the projected contact area can not be measured by use of optical microscope.

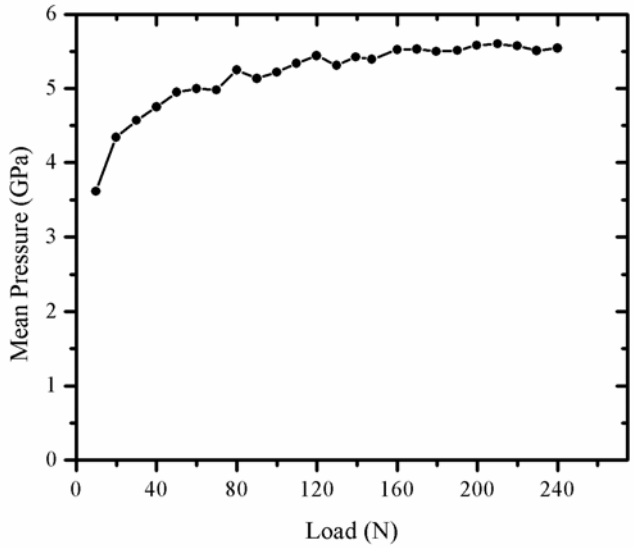

Fig. 5-2 Typical relationship between the mean pressure and the indentation load for BMG $Zr_{52.5}Ti_5Cu_{17.9}Ni_{14.6}Al_{10}$.

The relationship between P and d for the metallic glass is shown as a plot of $\lg(P)$ versus $\lg(d)$ in Fig. 5-3. As shown in the figure, the initial stage of the curve possesses a slope of about 2.5. According to the theory mentioned in Chapter 3, at the elastic stage of spherical indentation, the value of n should be close to 3. This indicates that even at a load as small as 10 N, plastic deformation, most likely, takes place beneath the spherical indenter. As the load is increased, the slope decreases and approaches 2 when the load increases to more than 150 N, indicating that the strain-hardening index x is about 0 at this stage, which agrees with the perfectly plastic properties of metallic glasses.

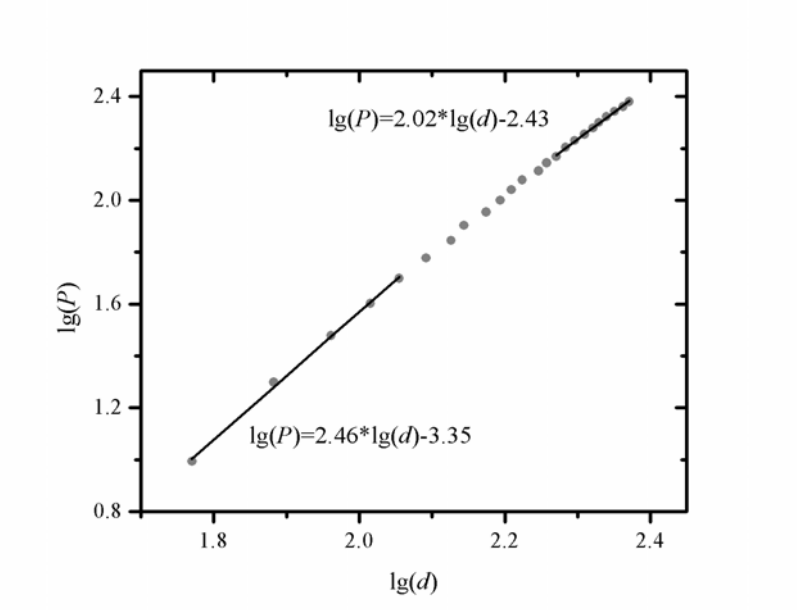

Fig. 5-3 Relationship between the indentation load and the contact circle diameter for BMG $Zr_{52.5}Ti_5Cu_{17.9}Ni_{14.6}Al_{10}$.

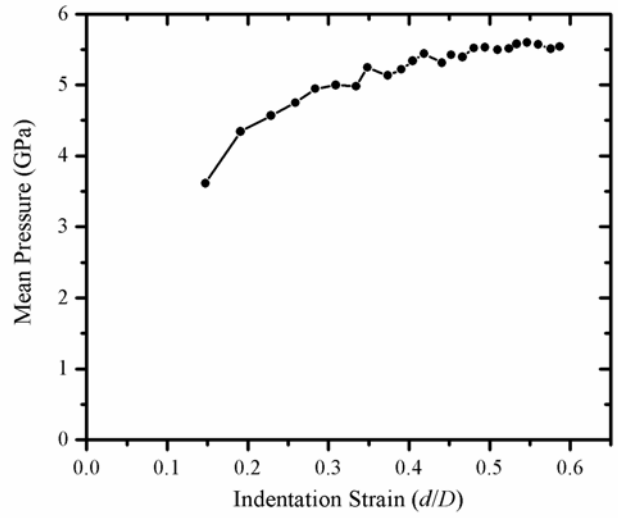

Fig. 5-4 Typical relationship between the indentation stress and indentation strain for BMG $Zr_{52.5}Ti_5Cu_{17.9}Ni_{14.6}Al_{10}$.

The spherical indentation behaviour can also be plotted as mean pressure versus indentation strain d/D, where d is the contact circle diameter and D is the diameter of the spherical indenter. Fig. 5-4 shows the indentation stress-strain relationship of the metallic glass, indicating a similar trend shown in Fig. 5-3.

The spherical indentation behaviour of metals has been extensively investigated. Tabor [4] indicated that for fully (or ideally) plastic metals, i.e., metals that were heavily worked and unable to strain harden further, the spherical indentation would undergo three stages: the elastic deformation stage, the transition stage and the fully plastic stage. Plastic deformation started when the mean pressure was larger than 1.1 times yield strength of the metal. After that, the mean pressure increased with indentation loads while the yield strength remained unchanged. When the mean pressure reached approximately 3 times yield strength, the fully plastic status was accomplished and this point was corresponding to d/D=0.1. Later, based on finite element simulation investigations by Mesarovic and Fleck [5], Herbert et al [6] proposed that this point was at $d/D \cong 0.16$.

Though both metallic glasses and heavily worked crystalline metals are ideally plastic, Fig. 5-4 indicates great difference between the spherical indentation stress-strain curves of them. For the metallic glass, the fully plastic status is reached at indentation strain around 0.4, far beyond the point determined in crystalline metals. While the mechanism behind is not clear, we propose two speculations here. One possibility is good elasticity of metallic glasses. During tensile and compressive tests, compared to crystalline metals, metallic glasses show very large elastic strain, usually more than 2% [3]. As a mechanical characteristic of metallic glasses, such elasticity will postpone the beginning of plastic deformation during spherical indentation and partially account for the large indentation strain of the fully plastic point. A second possibility is the different deformation mechanism involved in metallic glasses. Meyer's law is based on crystalline metals, which deform homogeneously when they are stressed. In metallic glasses, however, the plastic deformation is concentrated in the inhomogeneous shear bands and other parts only deform elastically.

5.3 Surface Morphologies upon Spherical Indentation

As mentioned in Chapter 3, spherical indentation can induce both elastic and plastic deformation, determined by the load or stress applied. During the elastic deformation stage, the material under the indenter fully recovers after the load is removed. In this situation, the specimen does not show any visible residual indentation impression. During the plastic deformation stage, however, the deformed material cannot fully recover and thus leaves a residual indentation impression on the specimen surface. Such residual impressions are usually used to calculate the hardness due to the "shallowing" effect, i.e., the material only recovers in the vertical direction and leave the contact area unchanged when the load is removed. In addition, the morphology of such impressions provides information about the indentation process.

Considering the accuracy of measuring the area of residual impression, which can be away from a circle shape at small indentation loads, we choose the minimum indentation load to be 10 N for the spherical indenter with radius of 200 μm. At this load, the residual impression inside the contact circle consists of two parts: the dark part and the bright one (see Fig. 5-5). This is because the indentation stress induced is not large enough to deform all the material beneath the indenter plastically. Under this situation, some of the material under the indenter recovers to horizontal plane and thus conducts a mirror reflection of light, or shows a bright image, as the free surface around the impression does. The permanently deformed part cannot conduct a mirror reflection and thus shows a dark image. The portion of dark part increases with the indentation load and covers the whole contact area at the load of 50 N (see Fig. 5-6). As the indentation load increases further, the morphology of the indentation impressions keeps similar before the fully plastic status is reached.

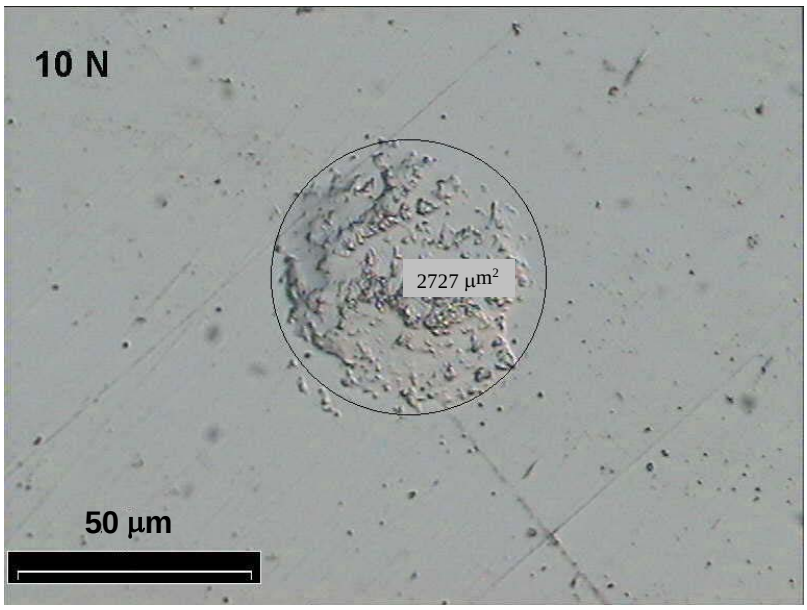

Fig. 5-5 Typical image of the spherical indentation impression on BMG $Zr_{52.5}Ti_5Cu_{17.9}Ni_{14.6}Al_{10}$ at the load of 10 N. (The perfect circle is used to estimate the contact area.)

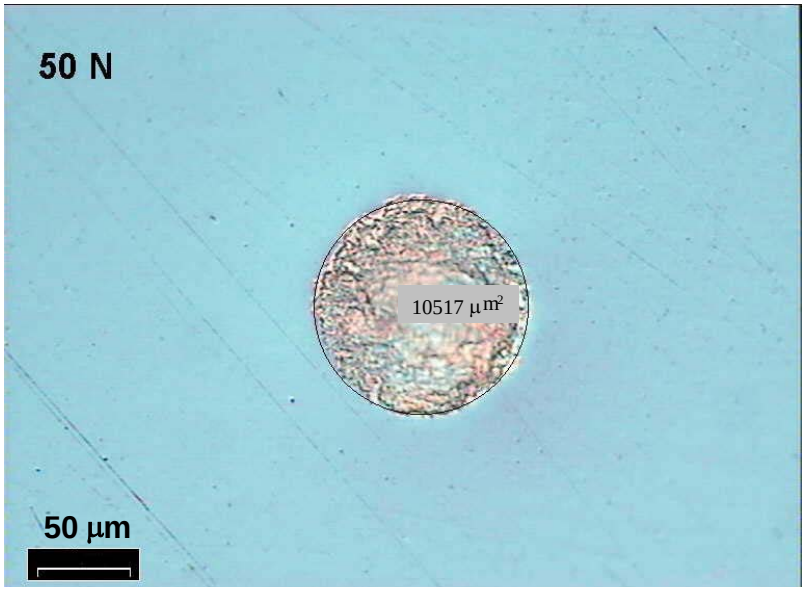

Fig. 5-6 Typical image of the spherical indentation impression on BMG $Zr_{52.5}Ti_5Cu_{17.9}Ni_{14.6}Al_{10}$ at the load of 50 N. (The perfect circle is used to estimate the contact area.)

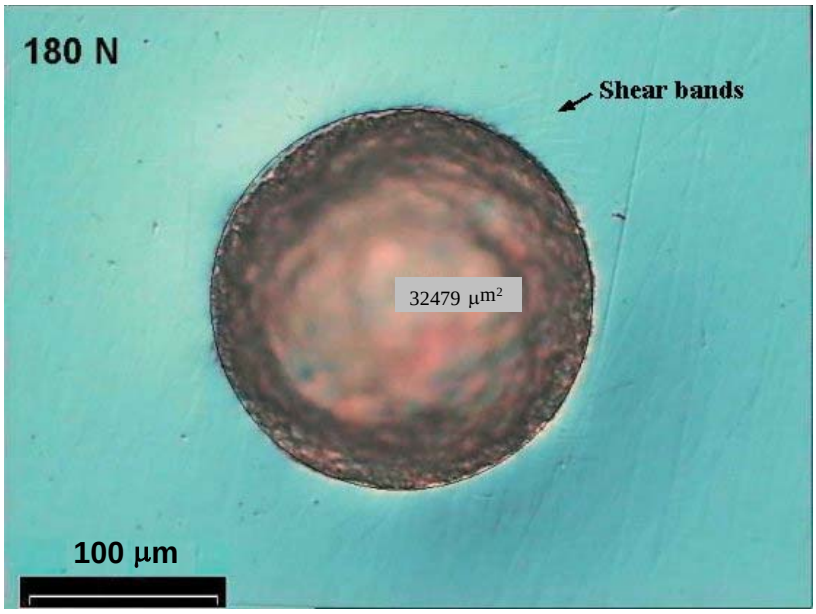

Fig. 5-7 Trace of shear bands around the spherical indentation impression. (The perfect circle is used to estimate the contact area.)

Though the fully plastic status is almost achieved at the load of 160 N, no apparent morphology change in the free surface is observed until the indentation load reaches 180 N. At the load of 180 N, a few shear bands are visible in the free surface around the indentation impression, as indicated by the arrow in Fig. 5-7. The shear bands become more significant as the load is increased. A typical image of shear bands (at the load of 230 N) is shown in Fig. 5-8. The shear bands originated from the periphery of the residual impression, where the maximum shear stress was located, and moved outwards in a spiral shape following directions of shear stresses in the free surface. On some spots, as indicated by arrows in Fig. 5-8, the shear bands initiated from the spherical indentation impression edge in two-prongs.

The reports on shear band morphology of metallic glasses upon spherical indentation were scarce before. Gilbert et al [7] performed depth-sensing spherical indentation on metallic glass $Zr_{41.2}Ti_{13.8}Cu_{12.5}Ni_{10}Be_{22.5}$ before and after annealing. They found ring cracks around the contact circle on the annealed metallic glass.

However, they did not study the shear band behaviour using spherical indentation. It should also be noted that the hardened stainless steel spherical indenter they used brought much inaccuracy into their depth-sensing indentation experiment. Because metallic glasses generally have a high hardness, a hardened steel ball is expected to yield when pushed against them.

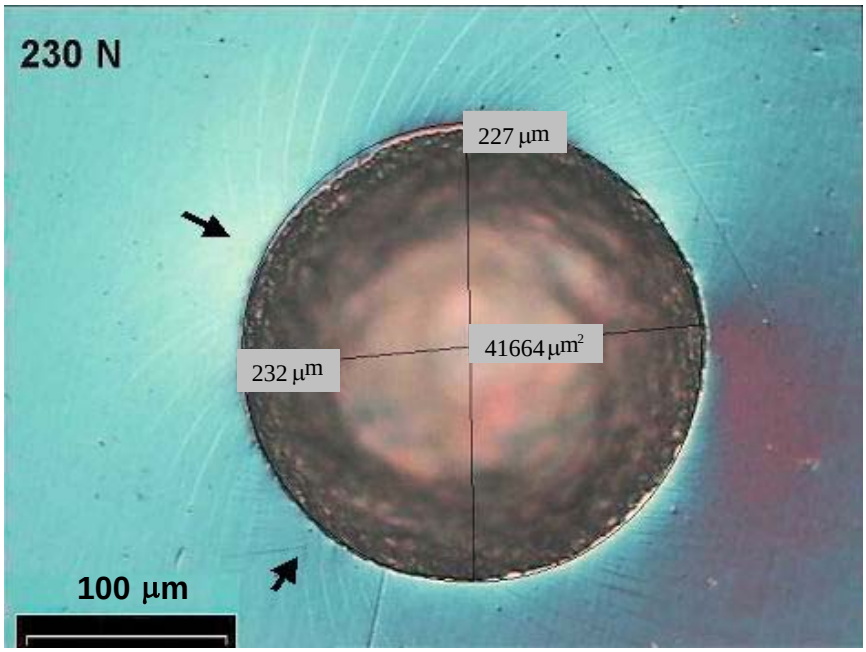

Fig. 5-8 Typical image of shear bands around the spherical indentation impression. The arrows indicate the spots where the shear bands expand in different directions.

The spiral shear bands were found around the impression of spherical indentation on nanocrystalline Fe by Malow et al [8], who used an automated ball indentation technique. It was determined that the shear bands emerged from the indentation at an angle of about 45° and at some spots they met each other at an angle of about 90°. Since the shear bands are spiral in shape, the included angle between them is not a constant relative to the radial distance from the impression edge, but increases with the radial distance. In present work, SEM image (JEOL 6700F) reveals that the angles between the shear bands are about 80° near the indentation impression edge (Fig. 5-9). As mentioned in section 4 of Chapter 3, in the case of elastic spherical indentation, the

stresses are pure shear and along 45° to the radii on the free surface around the indentation. However, when plastic deformation occurs, the stress field turns from elastic one into elastic-plastic one. In the elastic-plastic stress field, the radial stresses and hoop stresses on the free surface are not equivalent in magnitude and thus shear stresses may deviate from the direction of pure shear stresses in the case of elastic indentation. The radial stresses are larger than the hoop stresses and lead the shear stresses closer to the radial direction, which is qualitatively in agreement with the observation.

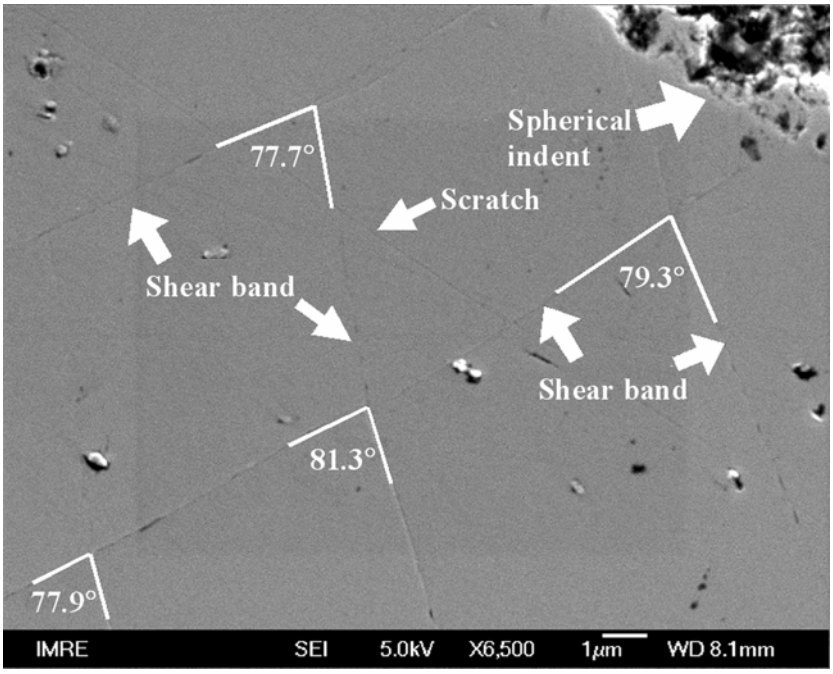

Fig. 5-9 Included angles between the pronged shear bands near the spherical indentation impression edge.

It is of interest to compare the spherical indentation behaviours of metallic glasses with those of non-metallic glasses, so we also performed spherical indentation on a soda-lime glass. As shown in Fig. 5-10, the indentation at the load of 33 N introduces ring cracks around the contact circle, which are representative characteristics of brittle materials subjected to spherical indentation [9, 10]. The ring cracks indicate that the

behaviours of brittle materials are dominated by principal stresses, not by shear stresses as in metallic glasses.

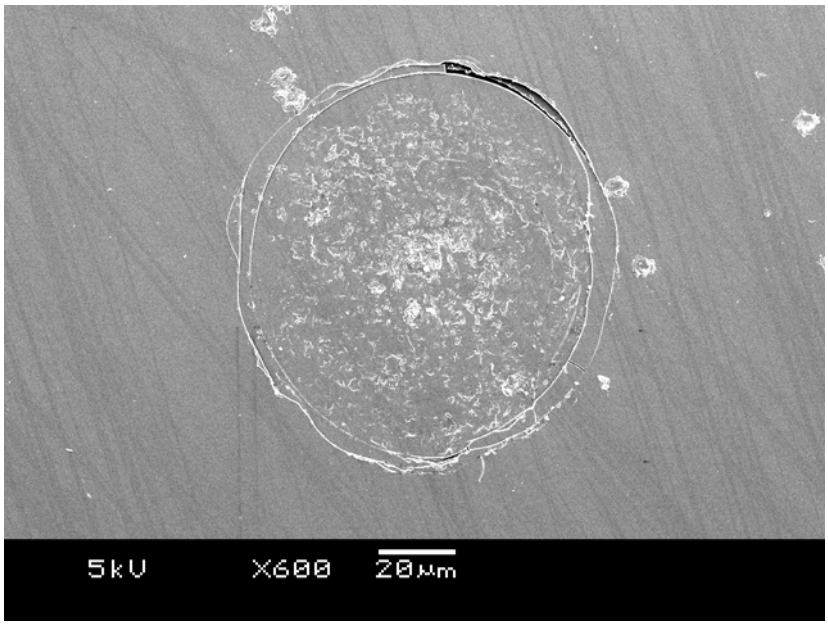

Fig. 5-10 Ring crack pattern around the spherical indentation impression on a soda lime glass.

5.4 Comparison between Spherical Indentation and Compression

Tabor [4] pointed out that for ideally plastic metals, the ratio of hardness to yield strength H/Y was around 2.8. According to this, the metallic glass should possess yield strength about 2 GPa when the final constant mean pressure is taken as the hardness. To better understand the spherical indentation behaviour, we conducted compressive tests at the strain rate of 10^{-4} s^{-1} on specimens with dimensions of $1.5\times1.5\times3$ mm^3 using Servohydraulic Testing Machine. The result of stress versus compressive extension shown in Fig. 5-11 indicates the fracture strength around 1.65 GPa, without apparent plastic elongation observed. Since metallic glasses generally fail soon after their yielding points, the fracture strength is very near to the yield strength, which gives the ratio H/Y of 3.3. This is similar to the results of Davis et al

[11-12], who studied several kinds of metallic glasses and found the ratio H/Y between 3 and 3.3 (Table 5-1).

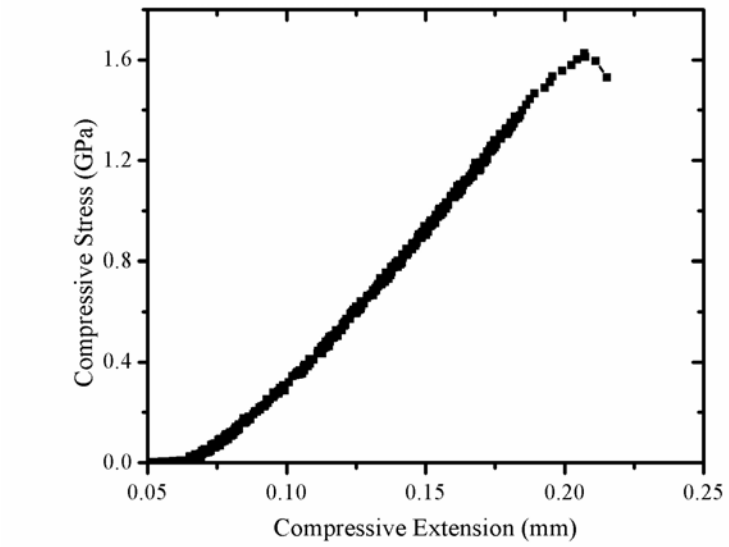

Fig. 5-11 Compressive test on BMG $Zr_{52.5}Cu_{17.9}Ni_{14.6}Al_{10}Ti_5$ at the strain rate of 10^{-4} s^{-1}.

Alloy	$Fe_{80}B_{20}$	$Fe_{80}P_{16}C_3B_1$	$Ni_{49}Fe_{29}P_{14}B_6Si_2$	$Pd_{77.5}Cu_6Si_{16.5}$
H/Y	2.97	3.35	3.26	3.17

Table 5-1 *H/Y* ratios of several metallic glasses. For $Ni_{49}Fe_{29}P_{14}B_6Si_2$, the yield strength is for tension tests [11-12].

There are mainly two theories on the ratio of hardness to yield strength of a material [12]. Based on the common observation on metals, one theory argued that $H \approx 3*Y$. Hill [13] provided theoretical justification for this observation based on slip-line field analysis. His theory applied to indentation on plastic-rigid body, where pile-up often takes place around the sides of the indenter, but it was indicated that this approximation also applied to materials where sink-in took place [12]. The other theory was proposed by Marsh [14-15], who argued that, for materials with ratio of Young's modulus to yield strength $E/Y < 133$, the hardness and yield strength had the following relationship:

$$H/Y = C + KB\ln Z \qquad (5\text{-}1),$$

where $B = 3/(3-\lambda)$, $Z = 3/(\lambda + 3\mu - \lambda\mu)$, $\lambda = (1-2\upsilon)Y/E$, $\mu = (1+\upsilon)Y/E$, and υ was the Poisson's ratio. He found empirically that *C*=0.28 and *K*=0.60. Marsh's theory applied well to covalently bonded network structure, such as oxide glasses.

For metallic glasses, the E/Y ratio is around 60, far less than 133. Whang et al [16] studied the ratios of hardness versus Young's modulus of some metal-metal and metal-metalloid glasses and found that there was a linear correlation between the hardness and modulus. Compared with crystalline metals, which had *H/E* ratio around 1/500, metallic glasses possessed much higher *H/E* ratio, near 1/10. Based on these observations and others on Zr-based BMGs, Wang et al [17] assumed that the bonding tendency of Zr-based BMGs was probably covalent. All the above suggests that Marsh's theory may apply to metallic glasses. According to Marsh's theory, however, Davis [12] showed that the ratio H/Y of metallic glasses should be around 2.5, far away from the observed values. Present result in our work also indicates that for metallic glasses, H/Y is around 3.

5.5 Nanoindentation around Spherical Indentation Impression

To investigate the effects of the residual impression of spherical indentation on the material, nanoindentations were conducted using Berkovich diamond indenter tip on UMIS-2000 at 40 mN on the free surface. The nanoindentations were placed from 20 μm to 240 μm away from the edge of spherical indentation impression produced by the Microforce Tester at 230 N. The nanoindentations were further examined under SEM (JEOL 6700F, Japan) and AFM.

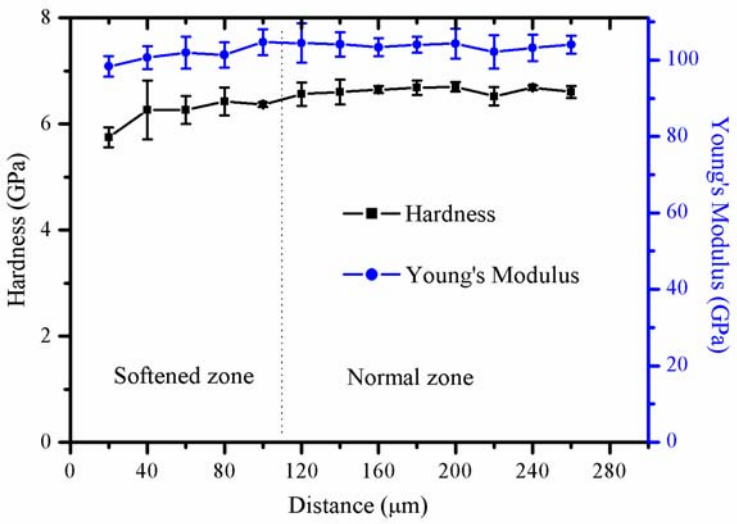

Fig. 5-12 Distribution of hardness and Young's modulus around the spherical indentation impression.

Fig. 5-12 shows the averaged values distribution of hardness and Young's modulus on the free surface as a function of the distance from the edge of the spherical indentation impression. At the load of 230 N, the material beneath the spherical indenter is fully plastic and the contact circle has a radius of about 110 μm (refer to Fig. 5-8). Fig. 5-12 reveals a softened zone around the residual spherical indentation impression. In this softened zone, the hardness and Young's modulus decrease in approach to the edge of the residual impression.

This phenomenon is quite different from that for crystalline metals. Tabor [4] measured the Vickers hardness on the free surface around the spherical indentation impression of various sizes (d/D) formed in mild steel and found that the Vickers hardness increased by more than 400 MPa in approach to the edge of impression. Later, by making surface and sectional explorations in annealed copper subjected to spherical indentation of various sizes, O'Neill [18] found that the zone around indentation had higher hardness and that larger spherical indentation sizes led to greater increase in the hardness. The above observations were based on metals that could strain harden during

spherical indentation. We conducted similar experiments, i.e., nanoindentations around spherical indentation impressions, on heavily worked steel and found no apparent relationship between the nanoindentation hardness and the distance from the spherical indentation impression. This result is not unexpected since the heavily worked steel is almost ideally plastic and spherical indentation does not bring further strain hardening to the material around the impression.

As mentioned in Chapter 2, it was found that [19] during indentation on metallic glasses, stress-induced phase transformation may yield nanocrystallines same as those produced by annealing metallic glass without deformation. It is proper to assume that such two kinds of nanocrystallines will influence the mechanical properties of specimen in the same way. However, nanoindentation behaviour of Zr-based BMGs showed that [17], compared to as-case metallic glasses, the annealed ones possess higher hardness. This implies that the apparent softening around the indentation impression does not arise from the phase transformation mechanism.

In order to determine the reasons for the apparent softening around the spherical indentation impression in the metallic glass, we chose some typical nanoindentation impressions in both the softened and the normal zone for details study. SEM and AFM images for the first nanoindentation impression (or the one nearest to the spherical indentation impression), the fourth, which is located in the softened zone where pre-introduced shear bands by the spherical indentation appeared, and the seventh, which is located in the normal zone where no pre-introduced shear bands appeared, are shown in Fig.5-13 (a)-(f). It is revealed that from the first to the fourth and further to the seventh nanoindentation impression, the dimensions of impressions or the “apparent” projected contact areas keep decreasing. During nanoindentations, such apparent contact areas are used to calculate the hardness. It is clear that the increase in

the apparent contact area is responsible for the apparent decrease of hardness and Young's modulus in the softened zone. On the other hand, however, in the softened zone, almost no or only small pile-up around the nanoindentation impressions is found (Fig. 5-13 (a)-(d)), while in the normal zone, large pile-up is found around the nanoindentation impressions. On one side of the nanoindentation impression located in the normal zone, the pile-up even extends to the corners (Fig. 5-13 (e)-(f)).

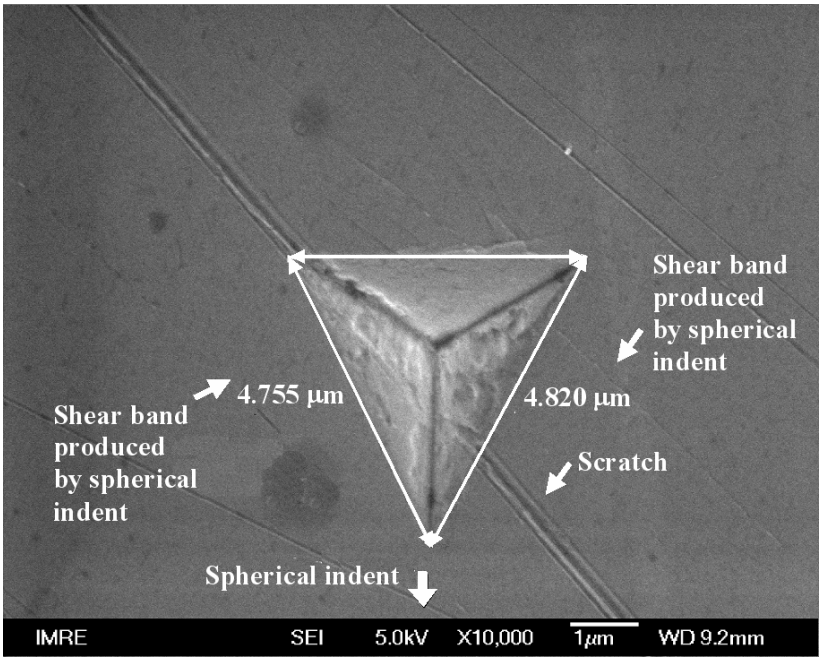

Fig. 5-13 (a) SEM image of the nanoindentation impression 20 μm away from the spherical indentation impression with radius of about 110 μm.

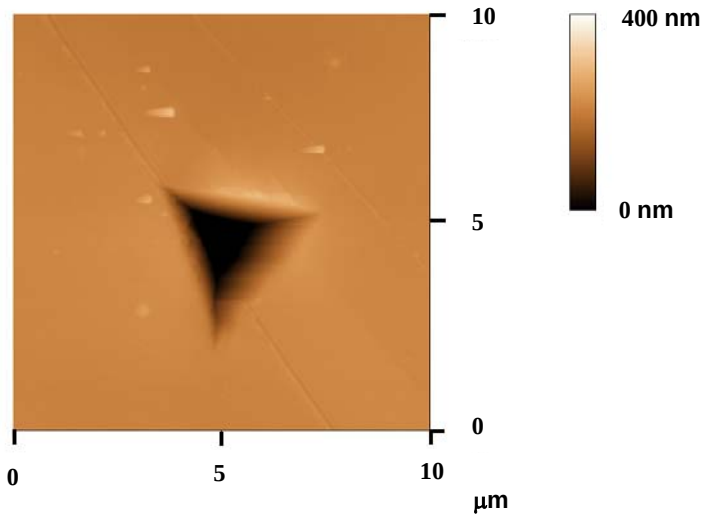

Fig. 5-13 (b) AFM image of the nanoindentation impression 20 μm away from the spherical indentation impression with radius of about 110 μm.

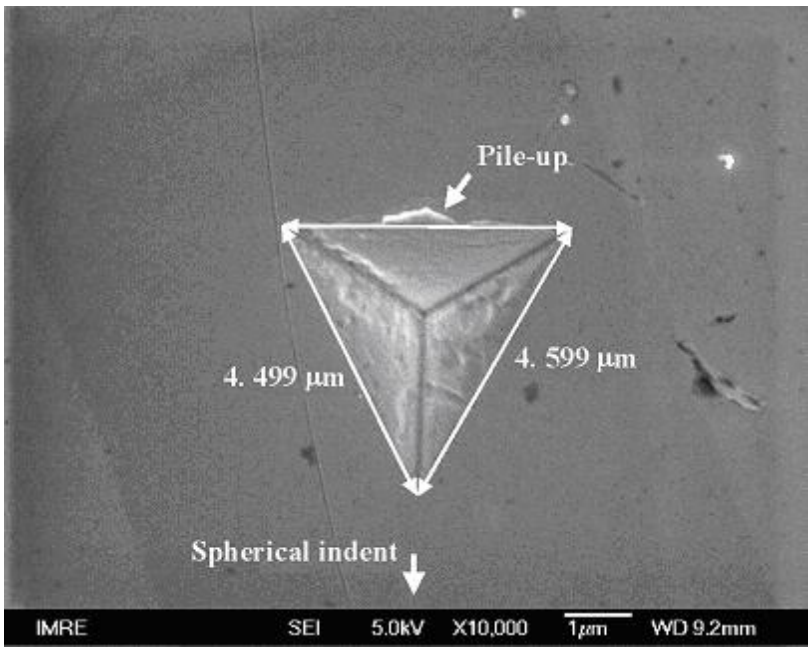

Fig. 5-13 (c) SEM image of the nanoindentation impression 80 μm away from the spherical indentation impression with radius of about 110 μm.

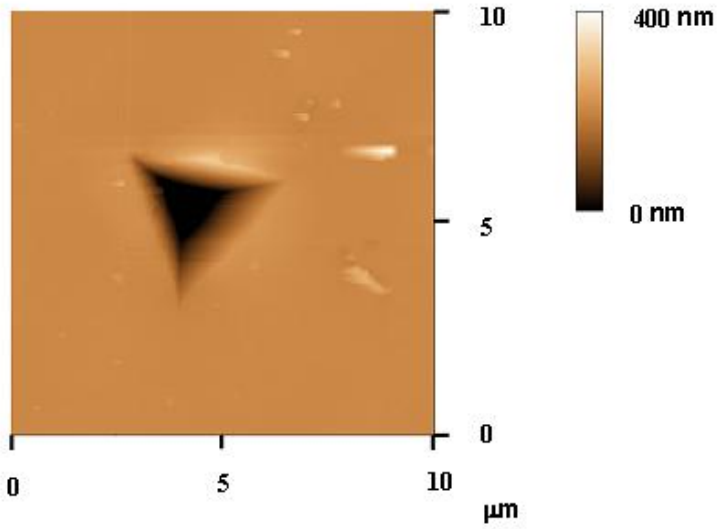

Fig. 5-13 (d) AFM image of the nanoindentation impression 80 µm away from the spherical indentation impression with radius of about 110 µm.

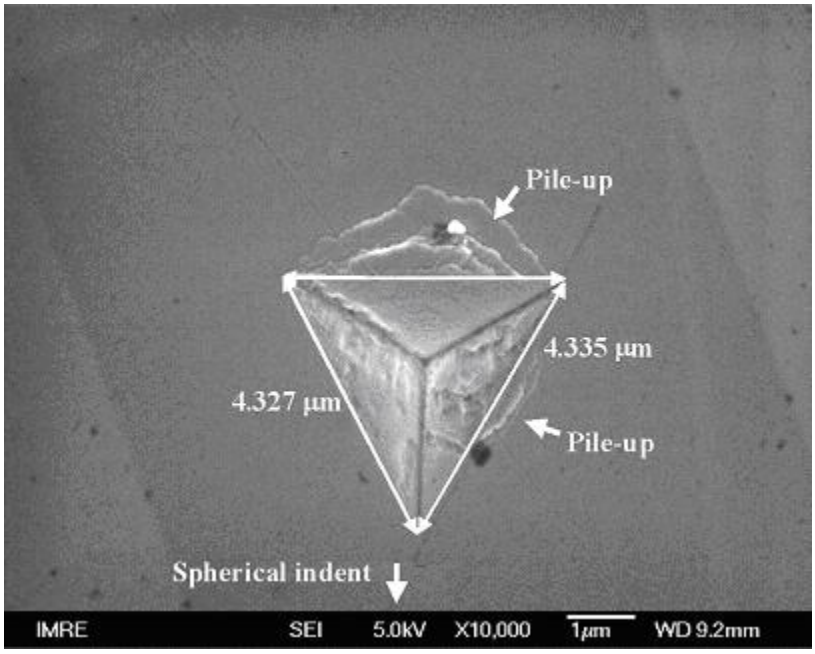

Fig. 5-13 (e) SEM image of the nanoindentation impression 140 µm away from the spherical indentation impression with radius of about 110 µm.

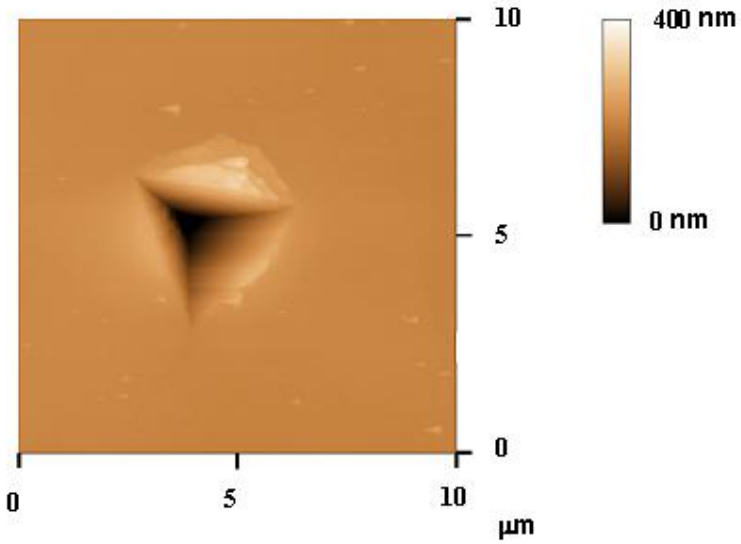

Fig. 5-13 (f) AFM image of the nanoindentation impression 140 μm away from the spherical indentation impression with radius of about 110 μm.

Pile-up is an important factor that influences the results and analysis of the nanoindentation tests, during which the projected contact area is deduced from the indentation depth. The influences of residual stresses on the measurement of hardness by nanoindentation were investigated by Tsui et al [20], who found that the conventional observation of the dependence of hardness on the residual stress state was due to the error in contact area calculation arising from pile-up that was caused by the residual stress. After taking pile-up into account, they found that residual stress did not affect the hardness.

In present work, it is clear that the pile-up around the nanoindentation impressions diminishes in approach to the spherical indentation impression. We think that the influence by residual stresses does not fully explain the phenomenon here as the metallic glass deforms elastically outside the shear bands and the stresses are released after the spherical indentation load is removed.

Takayama [21] investigated the drawing behaviour of $Pd_{77.5}Cu_6Si_{16.5}$ metallic glass wires and found that the plastic flow within the shear bands at the exit of the die did not continue and result in fracture due to work softening. Based on the observation that some shear bands were terminated by other bands, he proposed that this was due to the anti-action of work hardening resulting from the intersection of shear bands, which stopped the further movement of the shear bands. After drawing, the specimen with such pre-introduced shear bands exhibited more elongation and slightly higher fracture stress during tension tests. Later, Hagiwara et al [22] observed similar phenomena in drawn wires of metallic glass $Co_{72.5}Si_{12.5}B_{15}$. They studied the tensile strength and the fracture elongation for this alloy with various cold-drawn reductions in area and found that the strength and elongation increased till the area reduction reached about 60% and 30%, respectively. On the bending samples undergone cold drawing to 41% area reduction, they also observed that a large number of shear bands intersected each other and some shear bands were terminated by others. Kimura and Masumoto [23] attributed the enhanced elongation to local yielding in the pre-introduced shear bands and the higher fracture stress to the intersection of shear bands. However, it should be noticed that, as pointed out by Kimura and Masumoto [23], such work hardening was not intrinsic (physical) strain hardening, since an individual shear band was of an ideally plastic nature and the material outside the shear band possessed no plastic strain. It is of interest to note that such situation seldom occurs in metallic glasses subjected to uniaxial loading such as tension and compression tests, where shear bands rarely intersect with each other.

During indentation, pile-up usually takes place in ideally plastic materials and sink-in in strain-hardening materials. For ideally plastic materials, the part near the indenter is stressed and moves upwards around the indenter, forming pile-up. For strain-

hardening materials, the most stressed part near the indenter is hardened and moves downwards along with the indenter, forming sink-in. In the case of sink-in, the material far away from the indenter moves upwards and outwards. In our work, the metallic glass far away from the spherical indentation impression shows obvious pile-up during nanoindentation, exhibiting ideal plasticity. However, because of the ideally plasticity of metallic glasses, the disappearance of pile-up around nanoindentation near the spherical indentation impression cannot be caused by the intrinsic strain hardening. Since the pile-up (or plastic deformation) of metallic glasses takes place through shear band movement, we suppose that the pile-up disappearance is due to the intersection between the pre-introduced shear bands (by spherical indentation) and the new shear bands (by nanoindentation). Such intersection makes it more difficult for the new shear bands to move and for pile-up around nanoindentation to occur.

5.6 Serrated Flow Behaviour during Nanoindentation

When conducting low strain rate (3.3×10^{-5} s^{-1}) compressive tests on metallic glass $Pd_{40}Ni_{40}P_{20}$, Mukai et al [24] found the occurrence of multiple serrations on the stress-strain curves at a stress much lower than the apparent macroscopic yield strength. For the same alloy, Wright et al [25] also found serrations upon yielding during compressive tests at the strain rate of 10^{-4} s^{-1}. They attributed such serrations to the formation of shear bands and assumed that the formation of each shear band was manifested in a single serration [3, 25].

During Berkovich nanoindentations on the metallic glass $Pd_{40}Cu_{30}Ni_{10}P_{20}$ using instrument with high time and spatial resolution, Golovin et al [26] found serrations occurring on the *P-h* curves at low strain rates. They noticed the decrease of the serrations number with strain rate increasing and correlated this phenomenon with the

disappearance of serrated plastic flow above a certain strain rate during compression tests on the metallic glass $Pd_{78}Cu_6Si_{16}$. Based on the fact that shear bands still existed above that certain strain rate, they proposed that the serrations were not due to the shear band formation itself, but due to some kinetic peculiarities of elastic interaction of the shear front with the surrounding glass matrix. Later, Schuh and Nieh [27] investigated the serrated flow of several Pd-rich and Zr-rich metallic glasses during nanoindentations at different loading rates. Compared with Zr-rich metallic glasses, Pd-rich metallic glasses generally exhibited more serrated *P-h* curves at similar loading rates. For the same kinds of metallic glasses, the nanoindentation *P-h* curves were serrated at low loading rates but quite smooth at high loading rates. By plotting the strain rates against the indentation displacement, they found that at low loading rates, the figures showed some strain rate peaks, which were correspondent with the serrations on the *P-h* curves. After estimating the contribution of discrete shear bands to plastic deformation by removing all of the serrated parts from the loading portion of the *P-h* curve, it was clear that at very low strain rates, essentially all of the plastic strain experienced by the metallic glasses during nanoindentation occurred in a serrated form due to the motion of individual shear bands. They proposed that at very low loading rates, a few shear bands or even a single shear band could enough rapidly accommodate the applied strain and thus serrated *P-h* curves occurred; at high loading rates, many shear bands were required to operate at every instant in order to accommodate the applied strain and thus continuous plastic deformations or smooth *P-h* curves were observed. This proposal was supported by the observations of Jiang and Atzmon [28], who conducted Berkovich nanoindentations on metallic glass $Al_{90}Fe_5Gd_5$ at different loading rates and found that (i) at high loading rates, the *P-h* curves were smooth and many shear bands with small spacing formed around the

nanoindentation impression; and (ii) at low loading rates, the *P-h* curves were serrated and only a few shear bands with large spacing were observed.

On top of the studies on serrated flow mentioned above, we designed an experiment to support our assumption in section 5.4 that the vanishment of the pile-up around the nanoindentation impressions near the spherical indentation impression was due to the intersection between the pre-introduced shear bands produced by the spherical indentation and the new ones by the nanoindentations.

At room temperature, metallic glasses plastically deform in the form of inhomogeneous shear bands. During indentations, the plastic flow builds up around the indenter and forms pile-up. In section 5.4, if the residual shear bands by the spherical indentation intersected and suppressed the new shear bands, less new shear bands would operate to accommodate the nanoindentation strain, which meant that at the same loading rate, the *P-h* curves of nanoindentations near the spherical indentation impression would tend to be more serrated than those of nanoindentations far away from the spherical indentation impression.

Our nanoindentation experiments were conducted around a spherical indentation impression with radius of 130 μm, which was produced by an indentation at the maximum load of 260 N and displacement rate of 0.1 mm/min. A series of Berkovich nanoindentations at the load of 40 mN and loading rate of 0.02 mN/s were performed around the spherical impression using Nano Indenter XP (MTS, USA). As shown in Fig. 5-14, the nanoindentation pattern consists of seven lines with five nanoindentations in each line. The nanoindentations in each line are separated by 30 μm to avoid interaction and the lines are separated by 50 μm. The sampling rate was 5 Hz, which we found suitable for tracking the details of the indentation process.

Noting that nanoindentation lines (a) and (b) are within the zone of pre-introduced shear bands while lines (f) and (g) are beyond that zone (refer to Fig. 5-14), we therefore compared the nanoindentations located in lines (a) and (b) with those in lines (f) and (g). The loading portions of the *P*-*h* curves for typical nanoindentations in the four lines are shown in Fig. 5-15. At the loading rate of 0.02 mN/s, some small serrations occur on the curves (f) and (g). However, as expected, the serrations on curves (a) and (b) are much more frequent and pronounced.

During nanoindentations at a constant loading rate, the indentation strain rate is defined as $\frac{1}{h}\frac{dh}{dt}$, where h is indenter displacement and t is time. The strain rate is generally very large at the beginning of experiment since h is very small. It decreases as $1/h$ at finite depths and approaches a nearly stable value for very large displacements. For the nanoindentations shown in Fig. 5-15, the corresponding strain rates are plotted as a function of the displacements in Fig. 5-16. The strain rate peaks, which are found to correlate exactly with the serrations on the *P*-*h* curves in Fig. 5-15, reveal the bursts of rapid displacements during the nanoindentations. As Fig. 5-16 illustrates, the strain rate peaks for nanoindentation lines (a) and (b) are larger in number and more pronounced than those for line (g). The characteristics of strain rate curve for line (f) are similar to those for line (g).

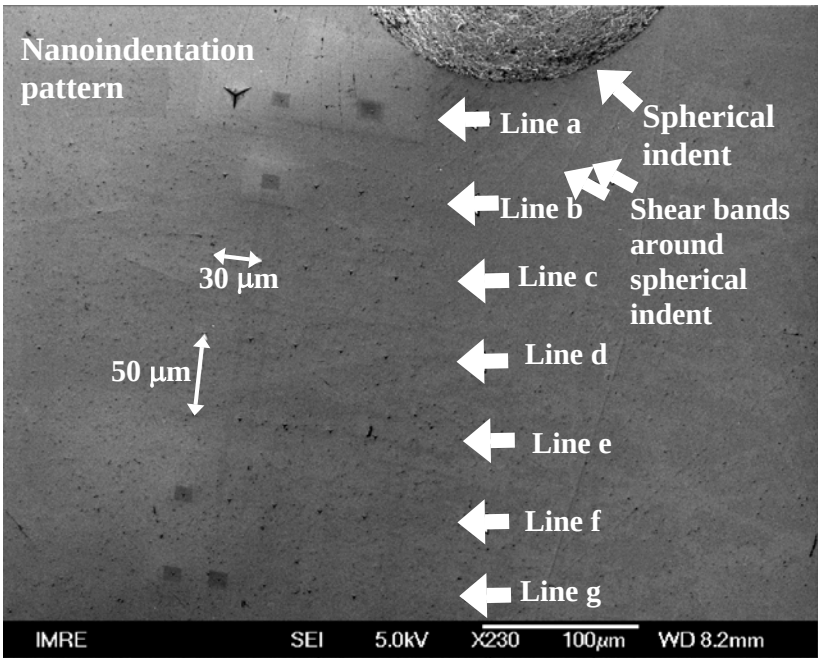

Fig. 5-14 (a) Nanoindentations around the spherical indentation impression with radius of 130 μm. (Line (a) contains only 4 nanoindentations at the load of 40 mN.)

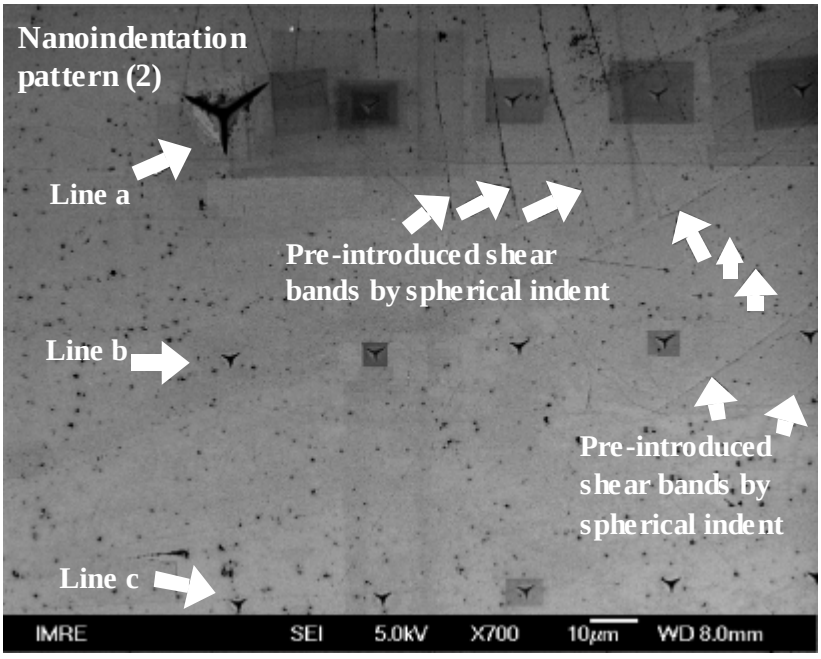

Fig. 5-14 (b) Lines (a) and (b) are in the pre-introduced shear bands zone near the spherical indentation impression; lines (f) and (g) are beyond the zone.

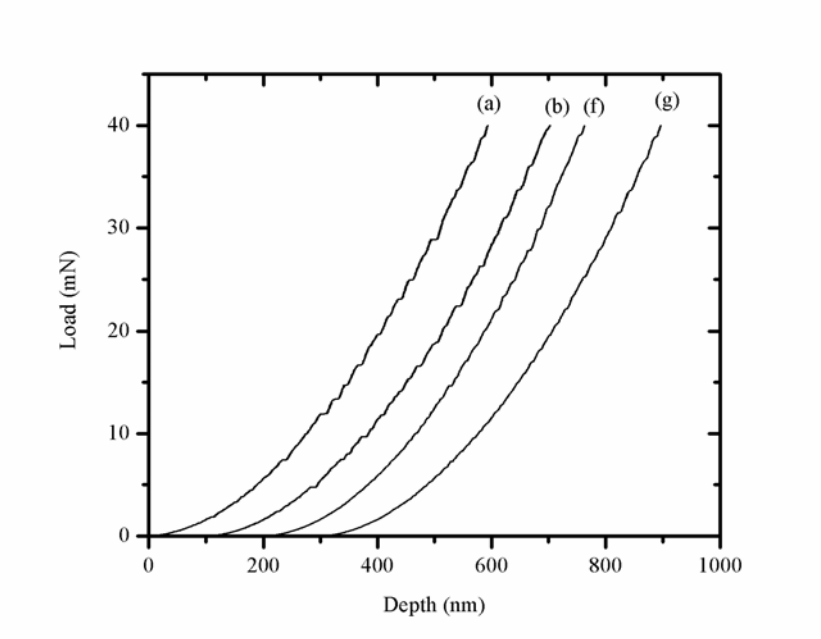

Fig. 5-15 *P-h* curves (during the loading portion) for nanoindentations at different distances from the spherical indentation. The curves for nanoindentations located in lines (a) and (b) are more serrated than those in lines (f) and (g).

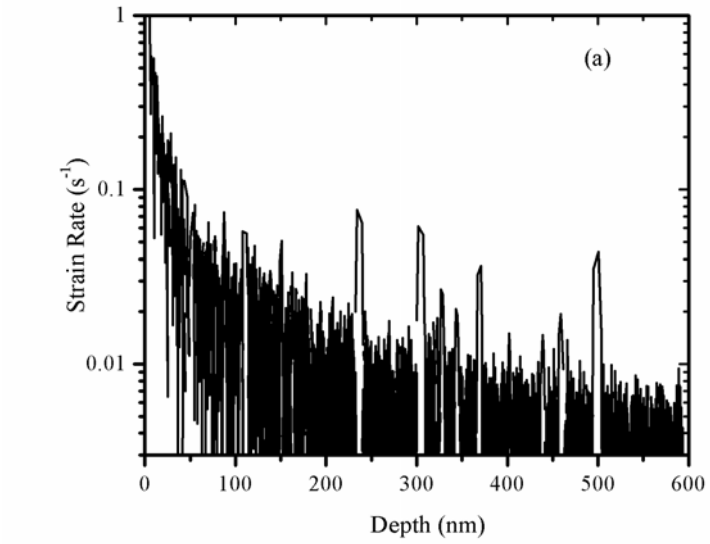

Fig. 5-16 (a) Figure of strain rate versus depth for nanoindentations in line (a), corresponding to curve (a) in Fig. 5-15.

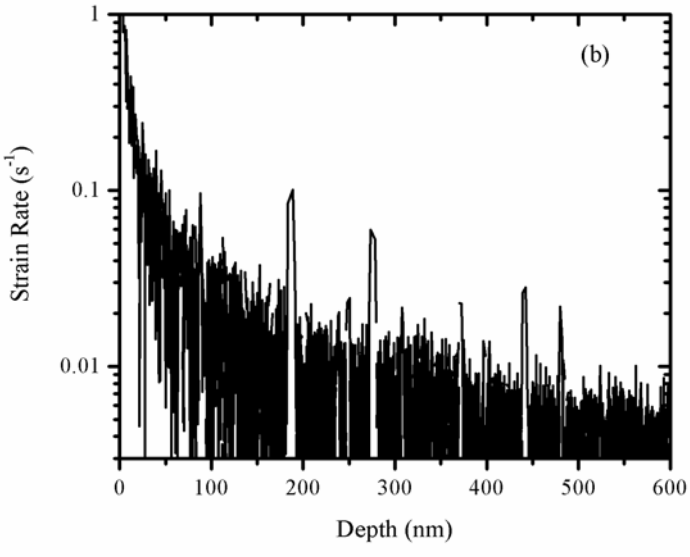

Fig. 5-16 (b) Figure of strain rate versus depth for nanoindentations in line (b), corresponding to curve (b) in Fig. 5-15.

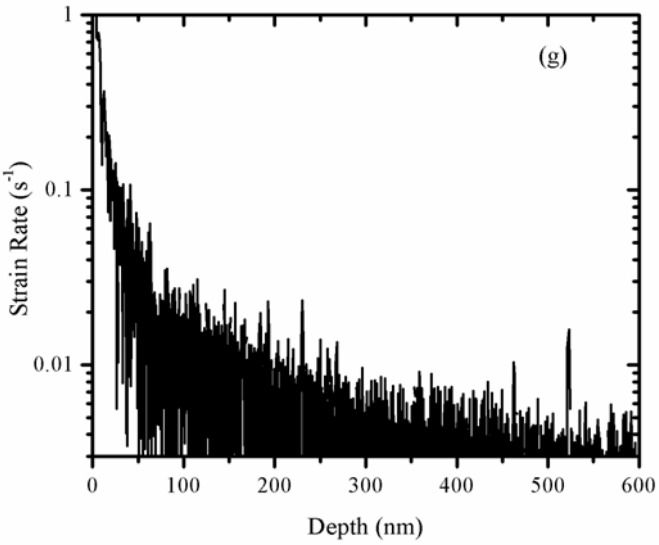

Fig. 5-16 (c) Figure of strain rate versus depth for nanoindentations in line (g), corresponding to curve (g) in Fig. 5-15.

Fig. 5-15 and Fig. 5-16 reveal that the plastic flows of nanoindentations near the spherical indentation impression are more serrated than those of nanoindentations far away from it. Since all the nanoindentations are conducted at the same loading rate, the difference in plastic flows during nanoindentations can be reasonably attributed to the different nanoindentation locations. This is consistent with our assumption that the

shear bands around the spherical indentation impression can intersect and suppress the nanoindentation shear bands. The above conclusion is also verified by our morphology investigations on the shear bands around the nanoindentations of which the strain rate curves are illustrated in Fig. 5-16. In Fig. 5-17, only a few shear bands are found on one side or two sides of the nanoindentations in lines (a) and (b); while around the nanoindentation in line (g), pronounced shear bands form on all the three sides.

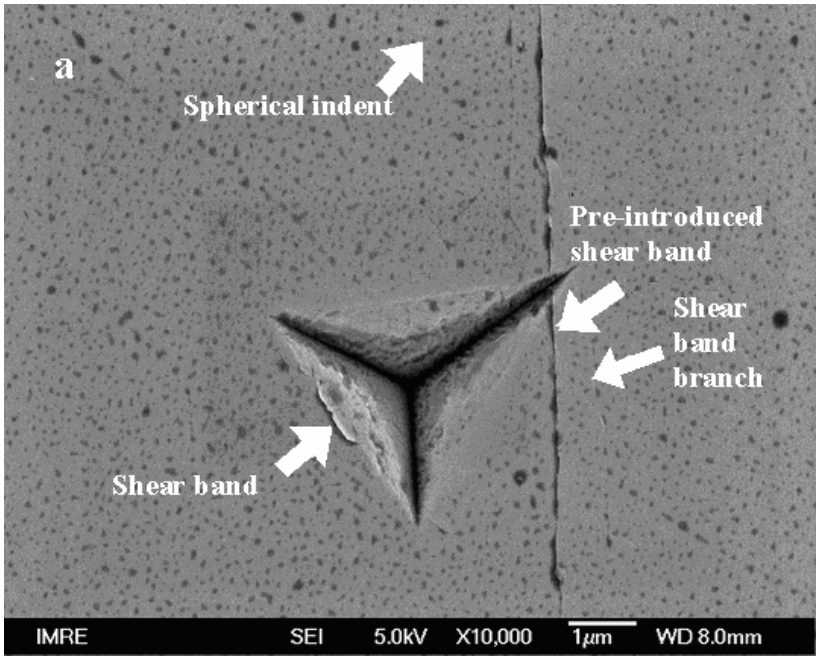

Fig. 5-17 (a) Nanoindentation in line (a) produced few shear bands around.

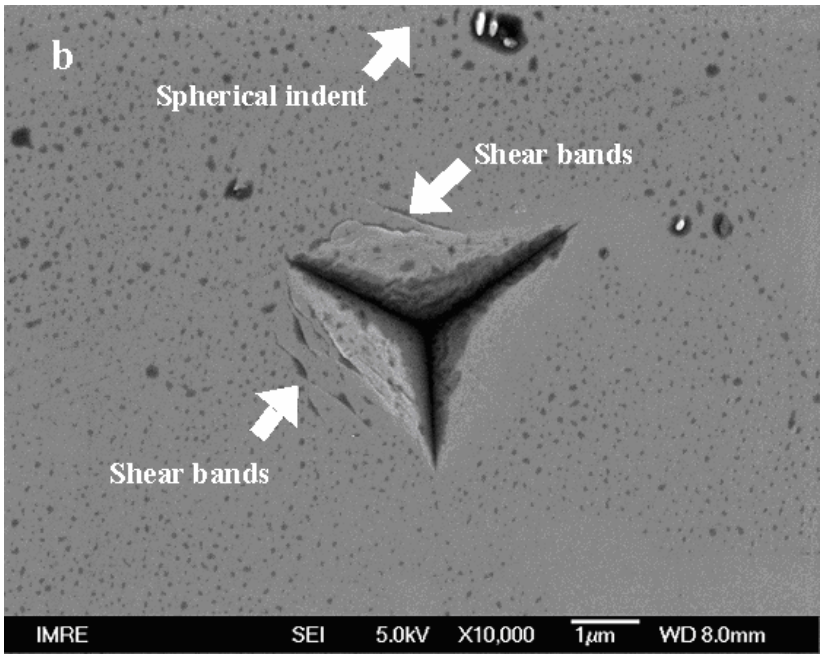

Fig. 5-17 (b) Nanoindentation in line (b) produced a few shear bands around.

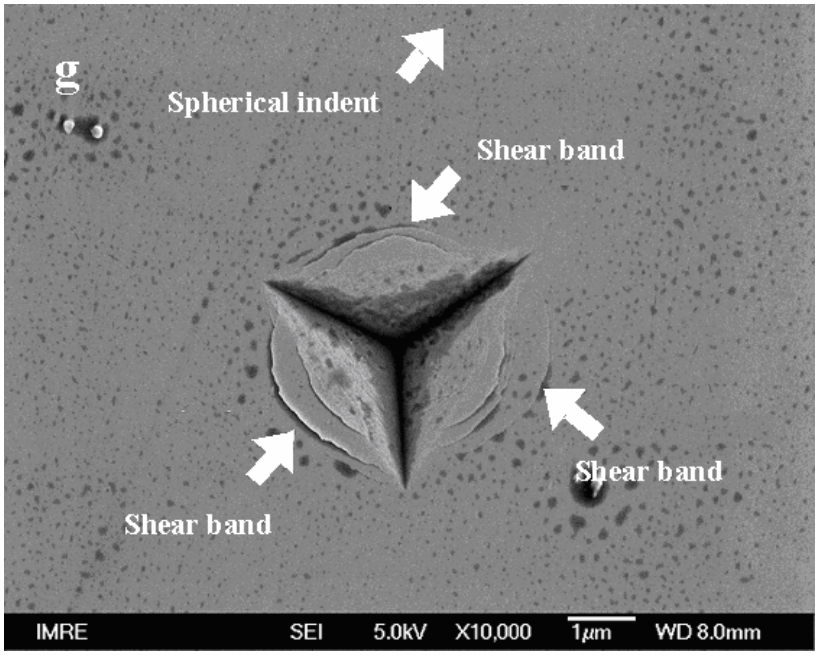

Fig. 5-17 (c) Nanoindentation in line (g) produced pronounced shear bands around each impression side.

Reference:

[1] Pekarskaya, E., Löffler, J. F. and Johnson, W. L., *Acta materialia*, **51**, 4045 (2003).

[2] Saida, J., Matsushita, M., Li, C., and Inoue, A., *Materials Science and Engineering A*, **304-306**, 338 (2001).

[3] Wright, W. J., Saha, R. and Nix, W. D., *Materials Transactions*, **42**, 642 (2001).

[4] Tabor, D., *The Hardness of Metals*, Oxford University Press, London (1951).

[5] Mesarovic, S. D. and Fleck, N. A., *Proceedings: Mathematical, Physical and Engineering Sciences*, **455**, 2707 (1999).

[6] Herbert, E. G., Pharr, G. M., Oliver, W. C., Lucas, B. N. and Hay, J. L., *Thin Solid Films*, **398-399**, 331 (2001).

[7] Gilbert, C. J., Schroeder, V. and Ritchie, R. O., *Metallurgical and Materials Transactions A*, **30A**, 1739 (1999).

[8] Malow, T. R., Koch, C. C., Miraglia, P. Q. and Murty, K. L., *Materials Science and Engineering A*, **252**, 36 (1998).

[9] Lawn, B. R., *Journal of Applied Physics*, **39**, 4828 (1968).

[10] Zeng, K., Breder, K. and Rowcliffe, D. J., *Acta Metallurgica et Materialia*. **40**, 2601 (1992).

[11] Davis, L. A., Ray, R., Chou, C. P. and O'Handley, R. C., *Scripta Metallurgica*, **10**, 541 (1976).

[12] Davis, L. A., *Scripta Metallurgica*, **9**, 431 (1975).

[13] Hill, R., *The Mathematical Theory of Plasticity*, Oxford University Press, London (1973).

[14] Marsh, D. M., *Proceedings of the Royal Society of London. Series A, Mathematical and Physical Sciences*, **279**, 420 (1964).

[15] Marsh, D. M., *Proceedings of the Royal Society of London. Series A, Mathematical and Physical Sciences*, **282**, 33 (1964).

[16] Whang, S. H., Polk, D. E. and Giessen, B. C., *Proceedings of the 4th International Conference on Rapidly Quenched Metals*, ed. by T. Masumoto and K. Suzuki, 1365 (1981).

[17] Wang, J. G., Choi, B. W., Nieh, T. G. and Liu, C. T., *Journal of Materials Research*, **15**, 798 (2000).

[18] O'Neill, H., *Hardness Measurement of Metals and Alloys*, The Thanet Press, Margate (1967).

[19] Kim, J. J., Choi, Y., Suresh, S. and Argon, A. S., *Science*, **295**, 654 (2002).

[20] Tsui, T. Y., Oliver, W. C. and Pharr, G. M., *Journal of Materials Research*, **11**, 752 (1996).

[21] Takayama, S., *Materials Science and Engineering*, **38**, 41 (1979).

[22] Hagiwara, M., Inoue, A. and Masumoto, T., *Materials Science and Engineering*, **54**, 197 (1982).

[23] Kimura, H. and Masumoto, T., in *Amorphous Metallic Alloys*, ed. by Luborsky, F. E., Butterworth, London (1983).

[24] Mukai, T., Nieh, T. G., Kawamura, Y., Inoue, A. and Higashi, K., *Intermetallics*, **10**, 1071 (2002).

[25] Wright, W. J., Schwarz, R. B. and Nix, W. D., *Materials Science and Engineering A*, **319-321**, 229 (2001).

[26] Golovin, Y. I., Ivolgin, V. I., Khonik, V. A., Kitagawa, K. and Tyurin, A. I., *Scripta Materialia*, **45**, 947 (2001).

[27] Schuh, C. A. and Nieh, T. G., *Acta Materialia*, **51**, 87 (2003).

[28] Jiang, W. H. and Atzmon, M., *Journal of Materials Research*, **18**, 755 (2003).

Chapter 6 Conclusions and Future Work

6.1 Conclusions

In this project we performed indentation studies on BMG $Zr_{52.5}Ti_5Cu_{17.9}Ni_{14.6}Al_{10}$. The BMG samples were obtained by arc melting of the pure elements into an alloy under Ar atmosphere and then the re-melted alloy was sucked into a water-cooled copper mould cavity of 1.5×5×30 mm^3 in dimensions. The samples were characterized by XRD and found to be amorphous.

Some of the samples were cut into appropriate dimensions and then polished to mirror smooth for indentation. Other samples were machined into 1.5×1.5×3.0 mm^3 for compressive tests.

Conventional spherical indentation tests using Microforce Tester were performed on the BMG samples by measuring the residual indentation impression. The mean pressures increased from 3.6 GPa to 5.5 GPa when the indentation loads increased from 10 N to 160 N and kept around 5.5 GPa when the loads further increased to 240 N. Such a trend in the mean pressures indicated that the deformation in the metallic glass gradually transforms from partially plastic deformation to fully plastic one. We did not observe fully elastic indentation using this conventional spherical indentation because elastic indentation does not produce visible residual impression. During fully plastic deformation, the material exhibited ideal plasticity, i.e., the mean pressures or indentation stresses kept stable upon increased indentation loads or indentation strains. This non-strain hardening behavior results from the non-crystalline structure of metallic glasses, which prevents the occurrence of dislocations.

In the fully plastic deformation stage of spherical indentations, shear bands in spiral shape were observed to expand outwards on the free surface around the residual

indentation impression. These shear bands generally followed the trajectories of the shear stresses on the free surface.

Compressive tests revealed that the metallic glass possesses yield strength around 1.7 GPa and a ratio of hardness to yield strength around 3.3. Though evidence indicated that the atomic bonding in Zr-based metallic glasses is possibly covalent [1], our results showed that Hill's [2] theory described the hardness-yield strength relationship more precisely than Marsh's [3-4] theory.

A series of Berkovich nanoindentations were performed using UMIS around the residual impressions of fully plastic spherical indentations and indicated an apparently softened zone around the residual impressions. Surface morphology imaging by SEM and AFM showed that out of the softened zone, pronounced pile-up occurred around Berkovich nanoindentations, while within the softened zone, the pile-up vanished as nanoindentations approached the residual spherical impression. The difference in hardness values within and out of the softened zone was attributed to the different morphologies around the nanoindentations since at the same nanoindentation load, pile-up caused less nanoindentation depth, less nominal contact area and thus higher nominal hardness. The vanishment of pile-up around the nanoindentations near the residual spherical indentation impressions was in turn attributed to the intersection between the new shear bands produced by the nanoindentations and the residual ones by the spherical indentation. Due to the intersection, less new shear bands could operate and move the material upwards around the nanoindentations, leading to less pile-up.

The behavior of shear bands in BMGs depends on strain rates. At high strain rates, many shear bands operate at the same time to accommodate the applied strain and thus the *P-h* curves of nanoindentations become very smooth. At very low strain rates, only

a few shear bands need to operate to accommodate the strain and thus the deformation is discontinuous, leading to serrated *P-h* curves [5]. Based on these observations, we performed nanoindentations around a fully plastic spherical indentation impression by use of Nano Indenter XP to verify our assumptions. The nanoindentations were conducted at the load of 40 mN and loading rate of 0.02 mN/s. The results indicated that the *P-h* curves of nanoindentations within the zone of residual shear bands were more serrated than those of nanoindentations far away from the residual spherical indentation impression. This phenomenon supported the conclusion that, at the same loading rate, less shear bands operated under nanoindentations within the residual shear bands zone because of the intersection between the new shear bands by the nanoindentations and the residual shear bands by the spherical indentation.

6.2 Recommendations for Future Work

In view of the results discussed above, some future work may be recommended. During the conventional spherical indentation by Microforce Tester, it is hard to investigate the elastic deformation. More work about the elastic deformation of metallic glasses can be carried out by depth-sensing spherical nanoindentations using UMIS. Since the elastic indentation does not produce any residual impression, the information can only be obtained from the *P-h* curves. Under this condition, precise calibrations of indentation load and depth are very important since the applied indentation load and depth are very small. Also, a good calibration of indenter tip shape should be carried out since the indenter tip shape parameters are involved in the calculations of mean pressures and indentation strains.

In this project, we have investigated the spherical indentation behavior and the influence of spherical indentation on the properties of the BMG. It may be of interest to apply finite-element simulation on the calculation of stress field under the spherical

indentation in metallic glasses and relate the quantitative stress status to the mechanical behavior of metallic glasses.

The interactions between the residual shear bands and the new shear bands have been investigated through indentation experiments. Further work can be carried out by using TEM to study the micro mechanism of such interactions.

Reference:

[1] Wang, J. G., Choi, B. W., Nieh, T. G. and Liu, C. T., *Journal of Materials Research*, **15**, 798 (2000).

[2] Hill, R., *The Mathematical Theory of Plasticity*, Oxford University Press, London (1973).

[3] Marsh, D. M., *Proceedings of the Royal Society of London. Series A, Mathematical and Physical Sciences*, **279**, 420 (1964).

[4] Marsh, D. M., *Proceedings of the Royal Society of London. Series A, Mathematical and Physical Sciences*, **282**, 33 (1964).

[5] Schuh, C. A. and Nieh, T. G., *Acta Materialia*, **51**, 87 (2003).